Theses and Dissertations

8-2014

Nanoscale Manipulation of Pristine and Functionalized Freestanding Graphene Using Scanning Tunneling Microscopy

Matthew Ackerman
University of Arkansas, Fayetteville

Nanometer Scale Manipulation of Pristine and Functionalized Freestanding Graphene Using Scanning Tunneling Microscopy

Nanometer Scale Manipulation of Pristine and Functionalized Freestanding Graphene Using Scanning Tunneling Microscopy

A dissertation submitted in partial fulfillment
of the requirements for the degree of
Doctor of Philosophy in Physics

by

Matthew Ackerman
Oklahoma State University
Bachelor of Science in Chemistry, 2004

August 2014
University of Arkansas

This dissertation is approved for recommendation to the Graduate Council.

_____

Dr. Paul Thibado
Dissertation Director

_____   _____

Dr. Laurent Bellaiche   Dr. Surendra Singh
Committee Member   Committee Member

_____   _____

Dr. Julia Kennefick   Dr. Ryan Tian
Committee Member   Committee Member

Abstract

Over the past ten years the 2D material graphene has attracted an enourmous amount of attention from researchers from across diciplines and all over the world. Many of its outstanding electronic properties are present only when it is not interacting with a substrate but is instead freestanding. In this work I demonstrate that pristine and functionalized freestanding graphene can be imaged using a scanning tunneling microscope (STM) and that imaging a flexible 2D surface is fundamentally different from imaging a bulk material due to the attraction between the STM tip and the sample. This attraction can be used to manipulate the graphene sample on atomic and even nanometer scales.

I first show that the electrostatic attraction between the tip and sample during imaging results in enhanced corrugation in the image. Next, I introduce constant-current spectroscopy measurements and demonstrate the ability to perpendicularly displace the graphene sheet at a single point over a range of tens of nanometers. An electrostatic model is then developed which characterizes the electrostatic force that is used to displace the sheet.

Finally, STM images and spectroscopy measurements, along with electron microscope images and molecular dynamics simulations, are used to characterize freestanding graphene sheets functionalized with platinum nanoparticles. It is shown that the platinum particles are self-organized but are not encapsulated by the graphene. Instead the nanoparticles are anchored to the sheet by a small number of covalent bonds. In the future the techniques shown here could be used to characterize other functionalized graphene systems.

Acknowledgements

I had the extraordinarily good fortune to join a truly exceptional research group as a first year graduate student at the University of Arkansas. I would like to sincerely thank my graduate advisor Paul Thibado for patiently guiding me through my graduate research and towards my career as a professional scientist, and for creating the supportive and creatively stimulating atmosphere found in our laboratory. I am also grateful for my fellow group members Peng Xu, Steven Barber, Kevin Schoelz, Dejun Qi, Gobind Basnet, Cameron Cook, and Josh Thompson, without whom my graduate career would have been many times more difficult and less enjoyable. The quality of my research was lifted by the work of our collaborators Drs. Salvador Barraza-Lopez, Yurong Yang, and Laurent Bellaiche at the University of Arkansas, Dr. Lifeng Dong at Missouri State University, and Drs. Mehdi Neek-Amal and Francois Peeters at the University of Antwerp, and I give them my gratitude.

I could not have completed my graduate work without the significant financial aid I enjoyed. My research was partially funded by grants from the National Science Foundation and the Office of Naval Research. I was also supported by the graduate assistantship offered by the Arkansas physics department and by the Doctoral Academy Fellowship awarded by the Graduate School.

I have received a tremendous amount of love and support from my family both before and during my time at Arkansas. I would particularly like to thank my parents for their constant encouragement through the ups and downs of my graduate career and for always providing a home when I needed one.

My greatest and most heartfelt gratitude is reserved for my best friend and partner Rani Achhireddy. Graduate school can be incredibly difficult and frustrating at times, and her

unwavering love and gentle encouragement saved me a thousand times over in the past four

years. I had an enormous amount of assistance as I worked on my dissertation but hers was all

that was necessary, and everything good in my life comes from our relationship. This

dissertation, and all of my work, is dedicated to her.

Table of Contents

I. INTRODUCTION

Graphene is a 2-dimensional (2D) crystal consisting only of sp^2-hybridized covalently bonded carbon atoms. Those atoms are arranged in a non-Bravais honeycomb lattice with two non-equivalent atoms per unit cell. In the case where the monolayer is locally flat it can be effectively described as an infinitely large polycyclic aromatic hydrocarbon. That is, the p-orbitals of every atom overlap with its neighbors and form one enormous conjugated system, making graphene an excellent electrical and thermal conductor. Long before its experimental isolation and characterization in 2004[1], graphene was studied theoretically both as a limiting case of few-layer graphite[2] and as a condensed-matter model of (2+1)-dimensional quantum electrodynamics[3]. In the absence of strong substrate interactions, graphene displays an extremely high intrinsic electron mobility with weak in-plane electron-phonon interactions[4]. In freestanding graphene out-of-plane flexural phonon modes strongly suppress the electron mobility at room temperature[5], but researchers recently reported micrometer-scale ballistic transport at room temperature in graphene when suppressing those modes by encapsulating it in hexagonal boron nitride[6]. Graphene has also been shown to be an excellent thermal conductor[7]. Despite being a monolayer, the strong in-plane covalent bonds in graphene protect it from tearing[8], and it is highly impermeable to gases[9]. This collection of unusual properties has produced a tremendous amount of excitement about the possibility of using graphene in a variety of devices, from computer processors to wearable electronics.

Landau[10], and later Mermin[11], famously argued that anomalously large thermal fluctuations in 2D crystals would result in such crystals being thermodynamically unstable at finite temperatures. It is now understood that 2D crystals are most likely stabilized by out-of-plane 3D rippling[12], and since 2004 several other 2D crystals, such as boron nitride[13], have

been isolated. However, the unique mix of extraordinary electronic and mechanical properties

present in graphene continue to attract intense attention from researchers and the experimental

characterization and manipulation of those properties looks to be an important and fertile branch

of condensed matter physics for years to come.

A. ELECTRONIC STRUCTURE OF GRAPHENE

Linear Electronic Dispersion and Massless Dirac Charge Carriers

The electronic structure of graphene is typically calculated using the tight-binding

approach[2,14]. This is a single-electron approximation in which the Hamiltonian, in the second

quantization formalism, is

$$H = -t \sum_{\langle i,j \rangle, \sigma} \left(c_{i,\sigma}^{\dagger} c_{j,\sigma} + h.c. \right) \tag{1}$$

Here, c $(c^{\dagger})$ is an annihilation (creation) operator, σ is the electron spin, $h.c.$ stands for

hermetian conjugate, t is the hopping integral, and the sum is taken to be over nearest-neighbor

sites. The hopping integral has units of energy and characterizes the probability of the electron to

tunnel from one lattice site to a neighboring one. This Hamiltonian can be thought of as a

phenomenological one in which the dominant term is identical to an isolated atomic Hamiltonian

plus a small perturbating term caused by the small but non-zero probability of the electron

tunneling from one site to another.

Fig 1 illustrates both the real and reciprocal lattices of graphene. The real lattice is shown in

Fig. 1a, with a dashed box drawn on the far right around a representative two atom unit cell.
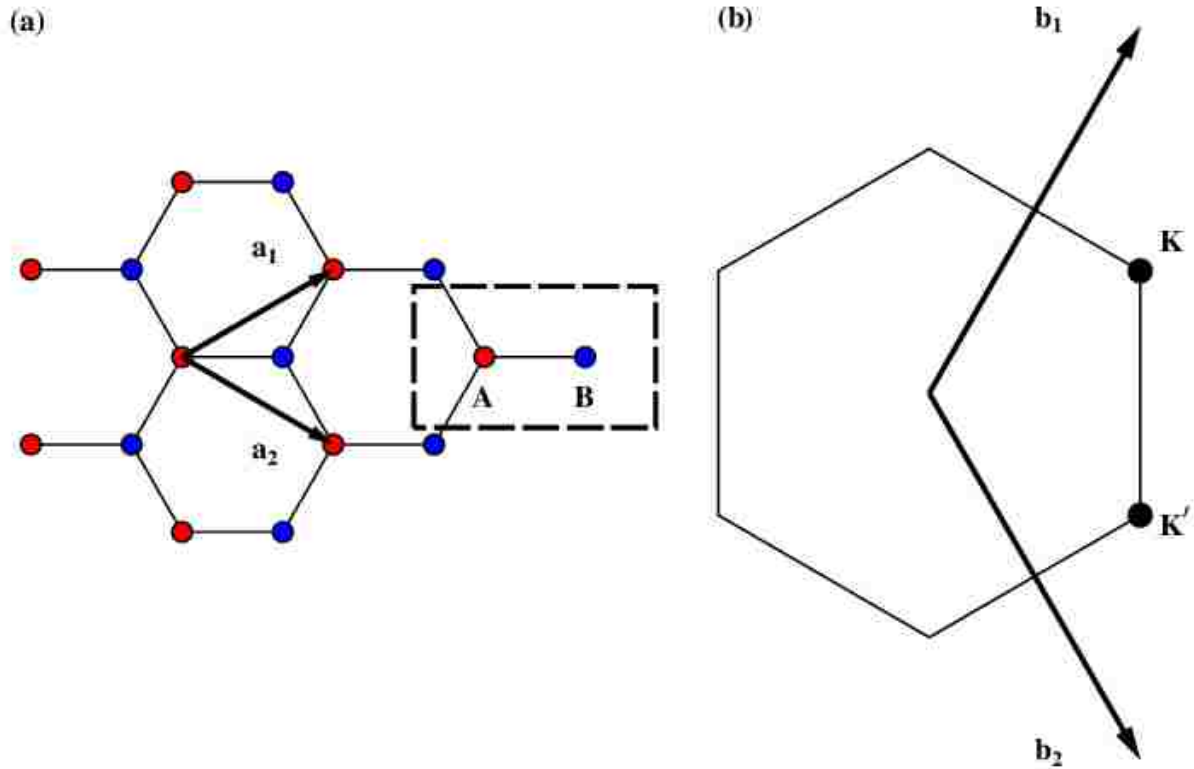
Figure 1: Representations of the real and reciprocal lattices of graphene. (a) The real-space lattice of graphene. The unit cell contains two sites, labelled A (red circles) and B (blue circles). There are two lattice vectors labelled $\mathbf{a_1}$ and $\mathbf{a_2}$ respectively. Lines are drawn between nearest neighbor sites as a guide. (b) The reciprocal lattice vectors and first Brillouin zone (BZ) of graphene. The black lines forming a hexagon define the BZ. The two reciprocal lattice vectors are labelled $\mathbf{b_1}$ and $\mathbf{b_2}$ respectively. Two important points of symmetry in the BZ, labelled K and K′ respectively and commonly referred to as the Dirac points, are represented by black circles.

These two sites are typically distinguished by the labels A and B, as done on the unit cell inside of the dashed box Fig. 1a. Throughout Fig. 1a the A sites are represented by a red circle while the B sites are represented by a blue circle. The lattice vectors are written in the following symmetrical form

$$\boldsymbol{a_1} = \frac{a}{2}(3, \sqrt{3}), \quad \boldsymbol{a_2} = \frac{a}{2}(3, -\sqrt{3}), \tag{2}$$

and are drawn and labelled on Fig. 1a. Here, $a = 1.42$ Å is the carbon-carbon distance. The reciprocal lattice vectors are then found to be

$$\boldsymbol{b_1} = \frac{2\pi}{3a}(1, \sqrt{3}), \quad \boldsymbol{b_2} = \frac{2\pi}{3a}(1, -\sqrt{3}). \tag{3}$$

These vectors and the Brillouin zone (BZ) they describe are drawn in Fig. 1b. It can be seen that the BZ is a hexagon. There are two particularly important points of symmetry in the BZ, the K and K′ points, which are labelled on Fig. 1b. Their positions in momentum space are

$$\mathbf{K} = \frac{2\pi}{3a}\left(1, \frac{1}{\sqrt{3}}\right), \quad \mathbf{K'} = \frac{2\pi}{3a}\left(1, -\frac{1}{\sqrt{3}}\right). \tag{4}$$

These points are commonly referred to as the Dirac points. There are two other sets of identical Dirac points in the BZ.

Each carbon atom in the graphene lattice contains four valence electrons. Three of these electrons are in orbitals of the form

$$|\psi_i\rangle = \frac{1}{\sqrt{3}}\left(|2s\rangle + \sqrt{2}|2p\sigma_i\rangle\right), i = 1, 2, 3 \tag{5}$$

where $|2s\rangle$ is the atomic $2s$ carbon orbital and the $|2p\sigma_i\rangle$ orbitals are atomic $2p$ orbitals directed along the lines which connect the carbon atom to its nearest neighbors. The carbon atom and its nearest neighbors are assumed to all lie in a plane, and these $2p\sigma_i$ orbitals are formed from appropriate linear combinations of the in-plane $2p_x$ and $2p_y$ orbitals. The three $|\psi_i\rangle$ orbitals are referred to as sp^2 hybridized orbitals, and the electrons in these orbitals form what are referred to

4

as σ (sigma) bonds. The hybridized orbitals are all mutually orthogonal and form bond angles of 120°. The fourth electron lies in the unmixed $2p_z$ orbital, which is oriented normal to the plane. The electrons in the unmixed orbitals form what are referred to as π (pi) bonds, and those electrons are commonly referred to as π electrons. The electrons in the hybridized orbitals are significantly lower in energy than the π electrons and do not contribute to the conductivity, thus justifying the validity of the tight-binding approximation when calculating the band structure of graphene.

The tight-binding Hamiltonian for graphene with only nearest-neighbor site hopping is

$$H = -t \sum_{\langle i,j \rangle, \sigma} \left(A_{i,\sigma}^\dagger B_{j,\sigma} + h.c. \right) \tag{6}$$

where A_i $\left(A_i^\dagger \right)$ is an operator that annihilates (creates) an electron on site $\boldsymbol{R_i}$ in sublattice A and B_i is an operator that acts in an identical manner in sublattice B. The hopping energy is found experimentally to be about $t = 2.8 \ eV$. This Hamiltonian gives, for the π electrons,

$$E_\pm(\boldsymbol{k}) = \pm t \sqrt{3 + 2\cos(\sqrt{3}k_y a) + 4\cos\left(\frac{\sqrt{3}}{2}k_y a\right)\cos\left(\frac{3}{2}k_x a\right)} \tag{7}$$

Near the **K** point, where $\boldsymbol{k} = \mathbf{K} + \boldsymbol{q}$ for $|\boldsymbol{q}| \ll |\mathbf{K}|$, Eq. (7) reduces to

$$E_F(\boldsymbol{q}) = \pm \hbar v_F |\boldsymbol{q}| + \mathcal{O}\left[\left(\frac{q}{K} \right)^2 \right] \tag{8}$$

Here, $v_F = 3ta/2 \approx 1 \times 10^6 \ m/s$ is referred to as the Fermi velocity and depends only on the local geometry and not, surprisingly, on the energy or momentum. This equation displays the famous linear electronic dispersion in graphene near the Dirac point. The plus sign in Eq. (8) refers to the π^* (conduction) band and the minus sign to the π (valence) band. Neglecting the higher terms (and next-nearest neighbor hopping), these bands are symmetric about $E = 0$ and come to a point at the Dirac point. Eq. (8) is formally identical to the solution to the massless

Dirac equation with the Hamiltonian described by Eq. (6)[3], which has led researchers to identify the charge carriers in graphene with massless Dirac particles. The massless nature of the charge carriers leads to several exotic electronic properties in graphene. For example, in the semiclassical approximation the cyclotron mass of a charged particle is[15]

$$m^* = \frac{1}{2\pi}\left[\frac{\partial A}{\partial E}\right]_{E=E_F} = \frac{E_F}{v_F^2} \tag{9}$$

where A is the area in k-space enclosed by the orbit. For a massive particle the energy will depend on the square of the velocity and the cyclotron mass is constant. Using Eq. (8) in Eq. (9), however, one obtains a cyclotron mass which is proportional to the wavenumber k_F and therefore, it can be shown, the square root of the electronic density. This relationship has been experimentally verified[16], as has the related half-integer quantum Hall effect phenomenon[17]. The electron-hole symmetry apparent in Eq. (8) also leads to Klein tunneling[18], in which charge carriers experience perfect transmission across a square potential barrier independent of barrier height.

Graphene Ripples and the Pseudomagnetic Field

The above analysis relies not only on the tight-binding approximation but also on the assumption that every carbon atom lies on a plane with its nearest neighbors i.e. that the graphene sheet was perfectly flat. It is well known, however, that freestanding graphene sheets feature intrinsic ripples around 0.5 nm in amplitude and $5 - 10$ nm in wavelength[12,19,20] that most likely allow the freely standing sheets to be thermodynamically stable. Even if it is assumed that this rippling has no effect on local carbon-carbon distances, the Hamiltonian described by Eq. (6) must be modified because the hopping energy t depends on the relative orientation of adjacent p_z orbitals. For example, in the absence of bending in the graphene sheet, adjacent p_z orbitals will be oriented parallel to one another. If the sheet is locally bent, however, those

6

orbitals will no longer be parallel and the hopping energy t will necessarily be modified.

Assuming a change of the form

$$t \rightarrow t + \delta t(\boldsymbol{r}) \tag{10}$$

an extra term will appear in the Hamiltonian,

$$\delta H = \sum_{\langle i,j \rangle, \sigma} \delta t_{ij}(\boldsymbol{r}) \left(A_{i,\sigma}^{\dagger} B_{j,\sigma} + h.c. \right) \tag{11}$$

Note that δt depends on the local geometry e.g. if one is examining an inflection point versus a stationary point, and therefore is a function of position in real space. Assuming that $\delta t(\boldsymbol{r})$ varies smoothly, it can be shown that this extra term can be written in the form[14]

$$\delta H = \sum_{\sigma} \int d^2 r [A(\boldsymbol{r}) A^{\dagger} B + h.c.], \tag{12}$$

where

$$A(\boldsymbol{r}) = \sum_{\vec{\delta}_{AB}} \delta t(\boldsymbol{r}) e^{-i\vec{\delta}_{AB} \cdot \boldsymbol{K}} = A_x + i A_y \tag{13}$$

Here, $\vec{\delta}_{AB}$ are the three vectors pointing from a carbon atom to its three nearest neighbors. Eq. (13) then defines a 2D vector potential

$$\boldsymbol{A}(\boldsymbol{r}) = A_x \hat{\boldsymbol{x}} + A_y \hat{\boldsymbol{y}} \tag{14}$$

Equations (12) and (14) can be used to rewrite the extra term in the Hamiltonian in the Dirac equation formalism[14],

$$\delta H = \int d^2 r [\hat{\Psi}^{\dagger}(\boldsymbol{r}) \boldsymbol{\sigma} \cdot \boldsymbol{A}(\boldsymbol{r}) \hat{\Psi}(\boldsymbol{r})], \tag{15}$$

The appearance of $\delta t(\boldsymbol{r})$ is formally identical to the coupling of the Dirac particles to a magnetic field $\boldsymbol{B} = (c/ev_F) \nabla \times \boldsymbol{A}$. Because of this formal connection, the effective field is commonly referred to as a pseudomagnetic field.

It is estimated that fields of up to 1 T are induced by the intrinsic rippling in graphene[21]. These fields can be increased in strength when external perturbations induce further strain in graphene. For example, in 2010 Levy *et. al.* grew highly strained graphene nanobubbles on a platinum surface and then used a scanning tunneling microscope (STM) tip to measure the induced Landau levels, revealing field strengths of up to 300 T[22]. This close relationship between local geometry and electronic properties points the way toward strain-engineering in future graphene based devices[23].

B. SYNTHESIS AND TRANSFER OF GRAPHENE FILMS

All methods of producing graphene involve extraction of the graphene film from a 3D structure on which the graphene was grown. It is commonly believed that the thermodynamic stability of the 2D surface is at least partially due to being locked into a metastable state while interacting with the 3D material[24]. The common semimetallic material graphite is naturally composed of a large number of graphene planes held together by van der Waals forces, and the first preparation of single layer graphene (SLG) was through the manual exfoliation of highly oriented pyrolytic graphene (HOPG)[1]. While manual exfoliation produces high quality flakes of SLG, those flakes tend to be only $\sim 1 - 10$ μm in size and the number of layers in the exfoliated graphene is difficult to control, making this technique unsuitable to the large-scale manufacture of SLG. Large ($> $ 1ft) sheets of graphene can be grown on metal substrates by chemical vapor deposition (CVD)[25,26]. In particular, the use of copper foil as a substrate in the CVD growth of graphene provides an inexpensive method of manufacturing large sheets of SLG[27]. The growth of epitaxial graphene on silicon carbide (SiC) through thermal decomposition is the most commonly used method of manufacturing extremely high quality single-domain SLG[28]. Finally, graphene can be synthesized through chemical routes such as

the *in-situ* reduction of graphite oxide in water[29], although the resulting graphene sheets tend to have inferior electronic properties compared to those grown by epitaxial means.

Once the SLG has been grown, it is typically advantageous to transfer it to a new substrate for either study or for application in a device. When manually exfoliating graphene from HOPG it is possible to press a freshly cleaved HOPG surface onto a silicon oxide (SiO_2) surface and, following exfoliation, have SLG flakes on the SiO_2 wafer[30]. A more general method of transfer involves depositing polymethyl-methacrylate (PMMA) on top of the graphene layer followed by the etching away of the original substrate. The PMMA/graphene can then be placed on the new substrate and the PMMA layer washed off with acetone[31].

It is often desirable to be able to study graphene free of any direct interactions with a substrate. Such interactions suppress the intrinsic electron mobility of graphene through mechanisms such as charge-induced scattering[32] and phonon scattering[33] and prevent any out-of-plane motion from occurring in the membrane. Graphene which does not interact with a substrate is commonly referred to as freestanding graphene. While SLG films must always be placed on some supporting structure, it is possible to study patches of freestanding graphene that, while macroscopically small, are several orders of magnitude larger than the lattice constant of graphene. There are several known methods for producing such samples. In 2008 Bolotin and coworkers chemically etched trenches below mechanically exfoliated SLG flakes on SiO_2 in order to measure the intrinsic electron mobility in graphene[34]. In 2009 Bunch *et. al.* exfoliated graphene on SiO_2 over pre-defined trenches in order to study the resonant properties of freestanding graphene[30]. SLG laid over pre-defined trenches in SiO_2 wafers has also been used to measure the intrinsic negative thermal expansion coefficient[35], thermal conductivity[7], and Young's modulus[36] of graphene. In addition, copper grids with micro-scale holes have been

used to obtain atomic-resolution transmission electron microscopy (TEM) images of graphene[37].

C. SYNOPSIS

This dissertation is primarily concerned with research related to imaging and manipulating pristine and functionalized freestanding graphene *via* scanning tunneling microscopy (STM). Following a brief overview of relevant STM principles, I will present direct evidence of the significant dynamic interaction between the STM tip and sample when imaging freestanding graphene at the atomic scale. Next, I will discuss single-point scanning tunneling spectroscopy (STS) experiments that exploit this interaction and provide relevant information regarding the elastic properties of freestanding graphene. Particular emphasis will be placed on the theoretical characterization of the electrostatic attraction between a biased STM tip and a grounded freestanding graphene sample as a complement to the experimental spectroscopy measurements. Finally, STM images and STS measurements will be combined with TEM images and molecular dynamics (MD) simulations in order to fully characterize freestanding graphene functionalized with platinum nanoparticles.

II. SCANNING TUNNELING MICROSCOPY

The scanning tunneling microscope was invented by Bennig and Rohrer, who shared the 1986 Nobel Prize in Physics for this work, and first implemented by Bennig, Rohrer, Gerber, and Weibel at the IBM Zurich Research Laboratory in 1982[38]. This device exploits the sensitivity of the tunneling current in a metal-vacuum-metal junction on the vacuum length[39] to map constant local density of state (LDOS) surfaces of conducting materials using a biased, atomically sharp metal tip held a few angstroms above the surface. It is capable of a lateral resolution of 0.1 nm and a perpendicular resolution of 0.01 nm[40] and is thus able to image surfaces with atomic resolution. Its inventors used this capability to directly image and therefore construct the real-space structure of the 7×7 reconstruction on the surface of Si(111)[41], a structure which had previously been subject to heavy debate, and atomic-resolution microscopy has since become a standard technique in the field of surface science[42,43]. Because it is capable of making atomic-scale measurements, spectroscopy measurements can probe local electronic structure[44,45], and individual atomic[46] and molecular[47,48] adsorbates can be imaged on surfaces. By reversing the polarity of the bias voltage, imaging and spectroscopy measurements can be made on the filled and empty electronic states almost simultaneously[49]. In addition to its capability as a tool for measurement, STM tips have been used to manipulate individual atoms and molecules, opening the door for the engineering of surfaces at the atomic level[50,51]. In the remaining portion of this chapter I will present a brief review of the theory and operation behind STM and describe the specific system used in my experiments.

11

A. STM OPERATION

Tunneling Theory

The classical problem of a particle with energy E interacting with a barrier of height U depends fundamentally only on whether $(E - U) > 0$ (unbound) or < 0 (bound). In quantum mechanics the probability of finding a particle of energy E in a particular point in space is given by a wavefunction that decays exponentially inside a barrier when $(E - U) < 0$, and for a barrier of finite width s there will always be a probability of finding the particle inside the classically forbidden region past the barrier. The non-zero probability of finding particles in the classically forbidden region is referred to as quantum tunneling and is one of the characteristically peculiar aspects of quantum mechanics. The experimental verification of this phenomenon played a historically important role in establishing the validity of quantum theory, and tunneling phenomena such as the ionization of hydrogen atoms in the presence of an external electric field (solved by Oppenheimer) and the emission of alpha particles from radioactive nuclei (solved by Gamow and independently by Gurney and Condon) played a critical role in the development of quantum theory.

We first consider a time-independent plane wavefunction of energy E and associated mass m which impinges on a one-dimensional square barrier of height V and width s. The solution given by the time-independent Schrödinger equation gives an exponentially decaying wave function $\psi(x) \propto e^{-\kappa x}$, with $\kappa = ik = \sqrt{2m(V - E)}/\hbar$ in the barrier region $0 \leq x \leq s$ and an attenuated wave function in the region past the barrier. Applying standard boundary conditions and assuming $E \ll V$, the transmitted probability current is

$$j_{trans} = j_{inc} \cdot \frac{16k^2\kappa^2}{(k^2 + \kappa^2)^2} e^{-2\kappa s}. \tag{16}$$

This simple model is typically only the starting point for more sophisticated treatments. However, some qualitative features, such as the exponential dependence of the transmitted current on barrier width, of Eq. (16) survive and are critically important to the operation of STM.

Twenty years before the invention of the STM, Bardeen developed a general expression for plane waves tunneling through a strongly attenuating potential from one metallic electrode to another[52], essentially utilizing time-dependent perturbation theory and Fermi's golden rule to argue that the tunneling current density was proportional to a constant (with respect to energy) overlap integral multiplied by the density of states in the final state. Soon after the invention of STM Tersoff and Hamann applied Bardeen's theory to the case of an atomically sharp metal tip interacting with a conducting surface[53] and argued, assuming a spherically symmetric (s-type) tip wavefunction, that the STM tunneling current is given by

$$I \propto \rho_s e^{-2\kappa s} \tag{17}$$

where V is the STM tip bias, ρ_s is the LDOS of the sample, $\kappa = \sqrt{2m_e\phi}/\hbar$, ϕ is the barrier height above the sample's Fermi level E_F, and s is the tip-sample separation. This simple picture has two very important consequences. First, the tunneling current is proportional to the LDOS. And second, that the current varies exponentially with the tip-sample separation.

The analysis that leads to the simple expression in Eq. (17) depends on a number of assumptions. First, it ignores band theory and assumes that there are empty states in the tip for electrons to tunnel into while conserving energy and momentum. Because the tip is metallic, in thermal equilibrium with the sample, and positively biased with respect to the sample (see Fig. 2), this assumption is generally valid. Second, it assumes a strongly attenuating barrier (where perturbation theory will be valid), and so STM imaging is typically conducted under low-bias conditions where E_F is well below the work functions of the tip and sample. Third, it assumes *s*-

13

type wavefunctions for the empty states at the tip, and this assumption is actually invalid for the metals (such as tungsten) typically used to make such tips and whose valence states have strong d-type character. Tersoff-Hamann theory was modified by Chen to take into account different symmetries for the tip wavefunctions[54], and other researchers have bypassed Tersoff-Hamann theory altogether by calculating the tip and sample states through alternate methods (such as density functional theory calculations) for use in Bardeen's formalism[55-59]. In all of these alternate approaches the tunneling current depends not only on the LDOS of the sample but also on the relative symmetries of the filled and empty states. However, the relationship between tunneling current and the sample's LDOS given by Eq. (17) holds as a rule of thumb, and the experiments discussed in this dissertation will not depend on a more detailed analysis.

The decay rate κ in Eq. (17) depends on the barrier height ϕ, and in the Tersoff-Hamann theory ϕ is assumed to have no dependence on lateral position nor on the tip-sample separation. It is known, however, that the actual form of the vacuum barrier during tunneling is not the trapezoidal barrier that is drawn with a solid line in Fig. 2(b), but is instead generally like the more rounded barrier drawn with a dashed line. This rounding is due to the interaction between the tunneling electrons and the metal surfaces which, classically, can be described by the addition of the image potential[60]

$$V_i(z) = -\frac{2.3(\ln 2)e^2}{16\pi\epsilon_0 d}\left[\frac{z}{d}\left(1-\frac{z}{d}\right)\right]^{-1} \tag{18}$$

where d is the distance between the image plains and therefore roughly equivalent to the tip-sample separation s. A classical potential, however, only approximates the actual one on the microscopic scales involved in STM, and detailed calculations taking into account quantum mechanical exchange and correlation energies, as well as the retarded potentials of the dynamic tunneling current and finite response time of charge in the metal surfaces, has shown that for $s \geq$
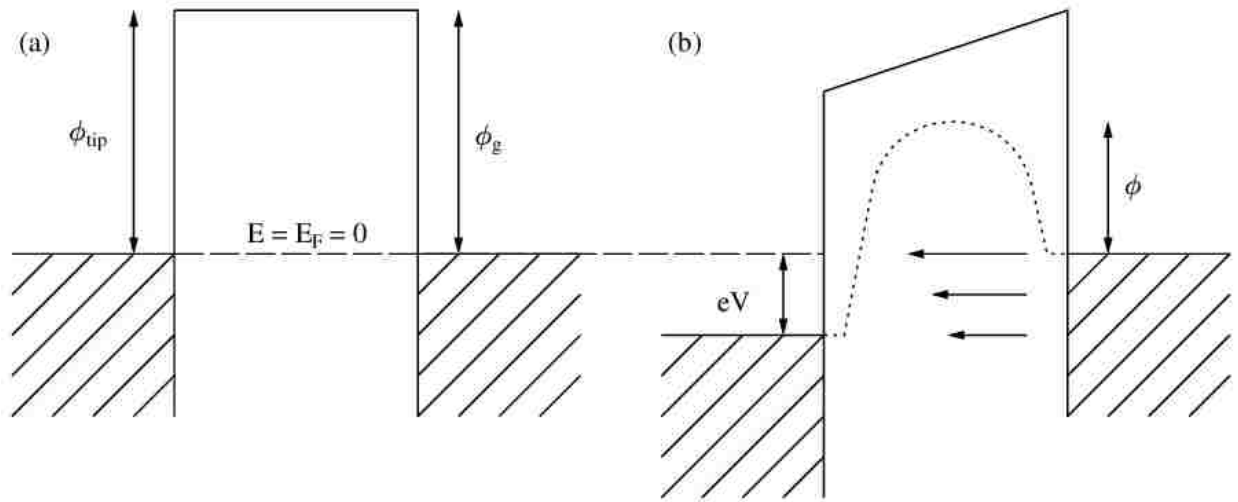
14

Figure 2: Schematic of the tip-vacuum-graphene junction in STM. (a) Junction with no voltage bias on the tip. The system is in thermal equilibrium so the Fermi levels (at the energy marked by the dashed line) in the tip and graphene are at the same energy. The work functions for the tungsten tip (ϕ_{tip}) and graphene (ϕ_g) are roughly equal, and the solid line shows the potential barrier between them. There is no tunneling current as the system is symmetric and the electrons at the Fermi levels have no empty states to tunnel into. (b) Junction with a positive bias *V* placed on the tip. This lowers the energy of the Fermi level in the tip by an amount *eV* relative to the electrically grounded graphene sample, where *e* is the fundamental charge. When tunneling occurs, the barrier changes from the trapezoid drawn with a sold line to the more rounded shape drawn with a dashed line due to the induced image potential. The barrier height ϕ experienced by the electrons tunneling from the Fermi level is noted. Horizontal arrows show the direction of motion for the tunneling electrons, with the arrow lengths proportional to the tunneling probability at that energy.

5 Å the effective barrier height ϕ is independent of s and is in fact the average of the two work functions during tunneling[61,62]. This result has been verified experimentally[63]. Because the tip-sample separation is typically in the regime $s \geq 5$ Å we consider the tunneling current to be purely exponentially dependent on s, and this exponential dependence is the key to the amazing resolution of which STM is capable.

STM Measurements

The characteristic measurement made using an STM is the constant-current imaging of a surface. In this mode a feedback circuit (described below) dynamically controls the perpendicular position of the STM tip as it scans across a surface at a constant rate such that the tunneling current is held constant. The data recorded then is a constant-current topography map of the surface. If the tip bias is held constant and conditions are such that Eq. (18) holds, that constant-current map is equivalent to a constant-LDOS map of the surface. In such a case it is possible, with a sharp tip and an atomically flat surface, for the STM to resolve the individual atomic orbitals on the surface, *i.e.* to achieve atomic resolution. The STM is therefore capable of resolving the real-space lattice of a surface as well as determining local defects, and this is the justification for referring to the constant-current topography maps as images. Imaging can also be performed by holding the height constant (feedback circuit off) and measuring the point-to-point tunneling current, but this technique is inherently unsuited to imaging the kinds of freestanding graphene systems discussed in this dissertation.

In addition to its imaging abilities, the STM can be utilized as an extremely sensitive atomic-scale probe at single points. Such measurements are commonly referred to as spectroscopic or STS measurements. For example, feedback off (constant-height) spectroscopy performed by recording the tunneling current while ramping through a voltage differential is a standard method

16

for measuring variations in the LDOS at some point along a sample[55,64]. Feedback on spectroscopic measurements are far less common in the literature but are critical to many of the experiments reported in this dissertation, and they will be more fully described in subsequent chapters.

B. DESCRIPTION OF SYSTEM

STM Chamber and Control

All experiments reported on in this dissertation were performed at room temperature using a low temperature STM (LT-STM) model manufactured by Omicron. A simple schematic of this STM is drawn in Fig. 3. The STM operates with the sample facing down and the tip pointing straight up as indicated in the figure. Measurements reported on throughout this dissertation are made with the convention that the z-axis is perpendicular to the sample surface and points toward the tip, so that increasing z corresponds to a downward tip movement. The sample in our system is always electrically grounded, and in the experiments described below the STM tip is held at a positive voltage bias V relative to the sample such that the tunneling current is due to electrons tunneling from filled states in the sample to empty states in the tip. The tunneling current is passed through an amplifier before arriving in the feedback circuit. When turned on, the feedback circuit compares the current I to the desired setpoint I_0 and, when $(I - I_0) \neq 0$, adjusts the z-position of the tip in the appropriate manner.

The motion of the STM tip is accomplished using piezoelectric crystals. Micrometer and larger scale positioning of the tip uses stick-slip piezoelectric actuators, while microscopic positioning uses a piezoelectric single-tube scanner. While in scan mode, the position of the tip in the xy plane is varied by tilting the tip as shown in Fig. 3 and is controlled completely by the computer. While imaging an $x \times y$ area of a sample, our system causes the tip to scan
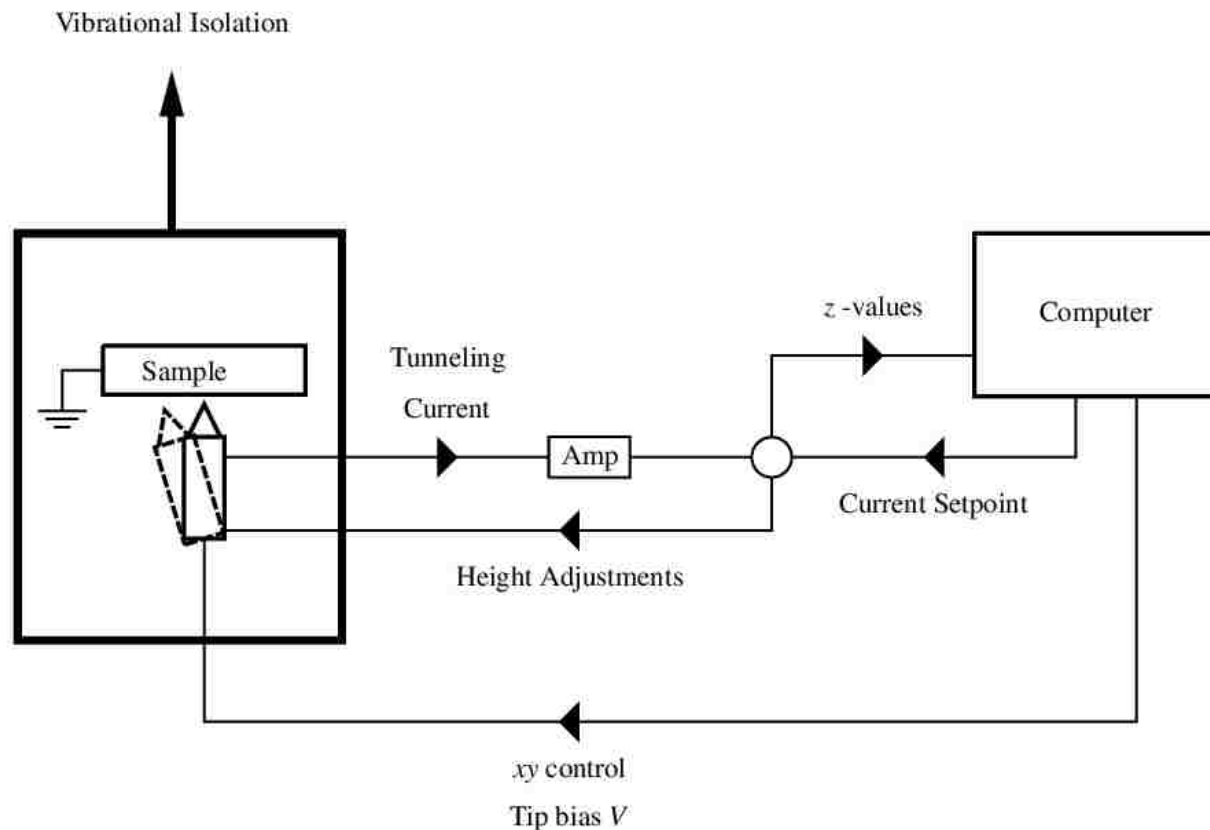
17

Figure 3: Schematic of the STM system. The tip and sample are under UHV in the STM chamber. The sample is grounded and is mounted such that the sample surface faces downward. The tip points up towards the sample. The tip-sample system is vibrationally isolated by a spring suspension system and the STM chamber by an active vibration-cancellation system (not shown). A computer located outside of the chamber controls the *xy* position of the tip, the tip voltage bias *V*, and the tunneling current setpoint. The tunneling current passes through the tip into an amplifier, and the amplified current is passed into the feedback circuit. If the feedback circuit is turned on, it compares the actual current to the current setpoint and adjusts the z-position of the tip accordingly. Tip height values are sampled during the scan and sent to the computer, and the computer uses those values to generate the image.

continuously in the *x*-direction across the sample at a set scan rate given in nanometers per second. It then steps in the *y*-direction in such a way that 400 scan lines will ultimately be collected. The computer records the *z*-position of the tip at 400 equally spaced points along the scan line so that the resulting data set consists of a 400×400 matrix of *z*-values. These values are presented as an image by the computer, with a color scale mapped to the range of *z*-values in the data. This data can then be processed in a variety of ways, such as subtracting off a constant background or introducing a tilt.

During STM operation an ultra-high vacuum (UHV) is maintained in the STM chamber. The base pressure of the system is on the order of 10^{-10} mbar, with pressures typically rising to 10^{-9} mbar during experiments. Prior to use the system was baked at high temperature to remove adsorbed particles on the chamber surface. A turbopump is used to initially evacuate the chamber while an ion pump and sublimation pump are used in tandem to establish and maintain the UHV. The chamber is sealed such that once the UHV is established the ion and sublimation pumps, which operate without producing vibrations, maintain the pressure without use of the turbopump.

The data collected by the STM consists of sub-nanometer tip movements, and the tip-sample separation is typically less than a nanometer, so it is extremely important to isolate the sample and tip from outside vibrations. The staging area has an eddy-current damping mechanism and is attached to a spring suspension system with a natural frequency of 2 Hz. In addition, a vibration-cancellation system actively senses and negates vibrations acting on the STM chamber as a whole. Because of the small tunneling currents involved (~ 1 nA), it is also critical to remove any electrical noise from the system. To this effect, all components of the system derive noise free electrical power from an uninterruptible power supply (UPS), which is continuously charged by the building's power supply. The batteries in the UPS also provide a backup in case of

electrical failure in the building's electrical system. We have also had a personal grounding rod extending from the ground outside the building to our system, providing a clean electrical ground for the sample.

<u>Electrochemical Tip Etching</u>

Our STM tips are manufactured in-house from 0.25-mm-diameter, polycrystalline tungsten wire. In order to image at the atomic scale, the metal probe used in an STM experiment must be atomically sharp, *i.e.* ideally only one atom on the tip should interact directly with the sample. In addition, the tip needs to be mechanically stable such that the tip is not vibrating significantly. In order to generate sharp and stable tips, we have developed a reliable tip etching method[65]. The tips are electrochemically etched in a sodium hydroxide solution using a custom double-lamella setup with an automatic gravity-switch cutoff [66,67]. In addition, an etch stop is applied to the wire prior to etching so that the length of wire exposed to the etching solution is controlled[68]. After etching, the tips are gently rinsed with distilled water and then briefly dipped in a concentrated hydrofluoric acid solution to remove surface oxides[69]. The tip is then immediately transferred through a load-lock into the STM chamber. Because UHV is maintained in the chamber the tip may be stored there for extended periods of time. In order to determine the suitability of a newly etched tip for atomic-resolution imaging, it is typically first tested on an atomically flat HOPG sample kept in the chamber for such a purpose.

III. STM OF FREESTANDING GRAPHENE

A. SAMPLE DESCRIPTION

The graphene samples in this study were obtained through a commercial provider. The graphene was grown *via* CVD on nickel foil. After the growth, the sample was placed graphene-face down over ultrafine, 2000-mesh copper transmission electron microscopy (TEM) grids. The circular TEM grids are 3.05 mm in diameter and feature a scaffold of square holes 7.5 μm wide and bar supports 5 μm wide. The nickel was then etched away leaving the graphene behind on the copper TEM grid. The graphene is partially supported by the copper bars, with freestanding graphene found in the square holes of the grid. The graphene is reported by the provider to be from one to six monolayers thick with 60% to 90% coverage.

The high coverage was confirmed by scanning electron microscopy (SEM). Representative SEM images of the graphene on the TEM grid are shown in Fig. 4. From these images we estimate that 90% of the grid on our sample was covered in graphene. A large-scale image is shown in Fig. 4(a), with the copper bars and interstitial holes plainly visible. The black regions are areas where the graphene is not present. An image of the area inside the dashed box is shown in Fig. 4(b). This area displays both regions with and without graphene. The pristine nature of the graphene film was confirmed with energy dispersive X-ray analysis. A second sample with SLG grown directly on polycrystalline copper foil was used as a stationary control sample.

Prior to loading into the STM chamber all samples were mounted on flat tantalum STM sample plates using silver paint. The TEM grids could be mounted with the graphene side up or down with respect to the tantalum plate. When placing the TEM grid graphene-face down, the grid was elevated by a stand-off support so that the graphene would not come into contact with the sample holder. The STM tip could still access the freestanding graphene through the holes of
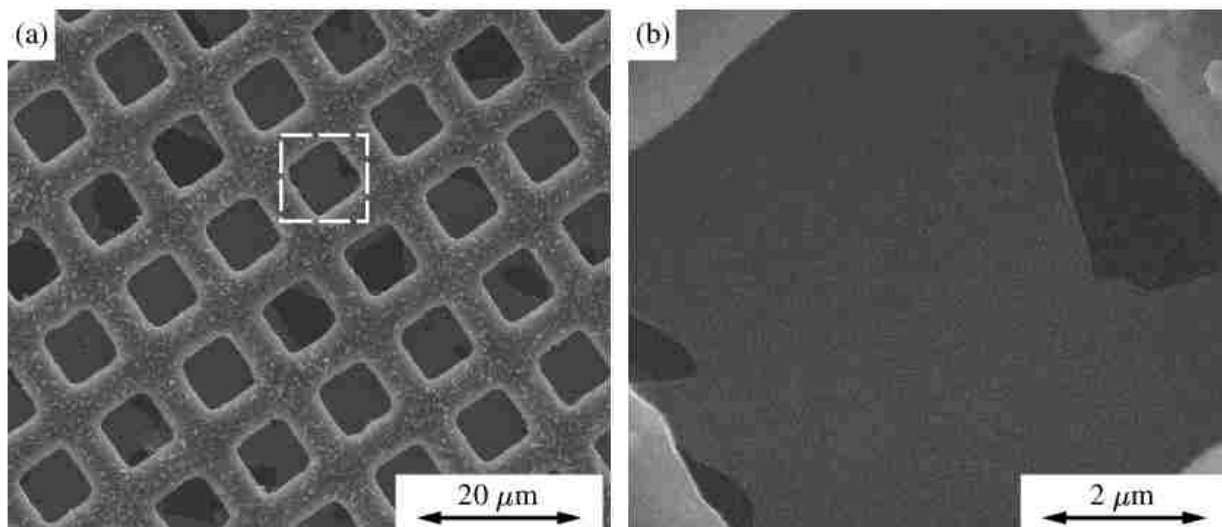
Figure 4: Representative SEM images of freestanding graphene on a 2000-mesh, copper grid acquired using an FEI Quanta 200 field-emission SEM equipped with a scanning TEM detector and an Oxford INCA 250 silicon-drift, energy-dispersive X-ray spectrometer. (a) Large-scale image of the graphene on TEM sample. The dark areas are locations where the graphene is not present. We estimate from these images that 90% of the TEM surface is covered with graphene. The interstitial hole marked by a white square is shown in detail in the image to the right. (b) Small-scale image of the area marked by the white square in the image to the left. The dark areas where graphene is not present are clearly visible. It is seen in this image that graphene can be found across most of the area of the hole.

the copper grid, and through trial and error we found this configuration produced superior images when compared to the graphene-face up configuration.

B. STM IMAGES

Enhanced Corrugations in Freestanding Graphene

Filled state constant-current 6 nm × 6 nm STM images of graphene on various substrates are shown in Fig. 5. A representative STM image of graphene on copper foil is shown in Fig. 5(a). This image displays a rather uneven morphology due to the copper foil, with the bright areas in the upper right- and left-hand corners at a height of a few nanometers above the dark area near the bottom of the image. However, the characteristic honeycomb structure of the carbon atoms in the graphene layer is still visible. The upper right-hand inset shows an atomic-resolution image from the central section of Fig. 5(a) around a single honeycomb ring, magnified two times, and displayed with a compressed color scale. Below the image is a height cross-section line profile extracted from the center of the STM image, showing an atomic-scale corrugation (d_e) of about 0.05 nm. A previous STM study done by our group with theoretical support from collaborators identified this corrugation height as the intrinsic variation in the electronic DOS of pristine graphene[70].

An STM image of the freestanding graphene is show in Fig. 5(b). The sample displays a curved topography with an overall height difference of 4 nm between the dark areas in the upper left- and lower right-hand corners and the brighter central portion of the image. The honeycomb structure is visible but less distinct due to the horizontal movement in the sample described below. Similar to the inset in Fig. 5(a), the inset highlights the atomic structure present in Fig. 5(b). It can be seen that the honeycomb structure is horizontally distorted. The line profile below the image reveals a corrugation amplitude of about 1 nm, 20 times larger than the electronic
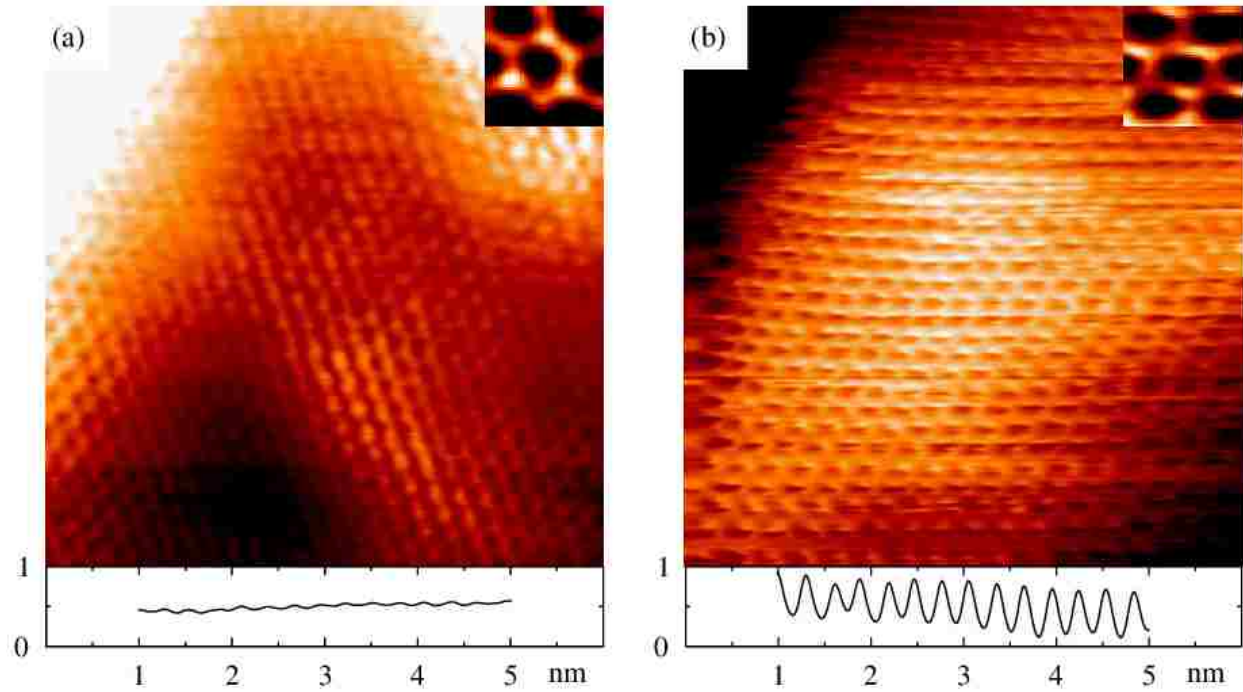
23

Figure 5: 6 nm × 6 nm filled-state STM images of (a) stationary graphene on copper foil and (b) freestanding graphene. Imaging parameters were $V = 0.1$ V and $I = 1.0$ nA. The insets in the upper-left of each image were cropped from the central region of their respective images, magnified two times, and displayed with compressed color scales. The graphs below each image are height cross-section line profiles of the atomic corrugations, extracted across the centers of their respective images. The two graphs use the same scale for direct comparison.

corrugation d_e and far too large to be attributed to atomic corrugations. Corrugation amplitudes

of up to 0.8 nm have been observed in STM images of HOPG and have been attributed to elastic

deformations induced in the graphite surface by the electrostatic attraction between the biased tip

and the grounded sample[71]. In order to investigate whether a similar phenomenon was

responsible for the anomalous corrugation in Fig. 5(b), a number of calculations were performed

which are presented below.

Tip-Graphene Interaction During STM Imaging

When the biased STM tip approaches a grounded conducting plane a new charge distribution

is induced in the plane and an attractive electrostatic force exists between the two surfaces. In

order to gain a qualitative understanding of how this force will vary as the STM tip scans across

the graphene surface, a collaborator performed tight-binding calculations within the self-

consistent Hückel method in which the tip was represented by a point charge held above the

graphene plane. The induced charge distribution in the plane was found when the point charge

was placed 0.1 nm directly above a carbon atom and when placed at the same height above a

hole. The Coulomb force was computed from the self-consistent charge distribution. The

calculations were performed for a 20 nm $\times$ 20 nm square patch of graphene containing more than

15,000 π electrons, and the results are summarized in Fig. 6. In Fig. 6(a) the charge distribution

in the plane is plotted in the case where the point charge was held above a carbon atom. The

induced charge distribution displays 3-fold symmetry, is greatest directly below the charge, and

drops to zero at an approximate radial distance of 1 nm. The charge distribution for the case

where the charge is held above the hole of a benzene ring is shown in Fig. 6(b). It displays 6-fold

symmetry but is otherwise similar to that of Fig. 6(a), with the important distinction that the

maximum induced charge is smaller. The two cases are directly compared in Fig. 6(c), which
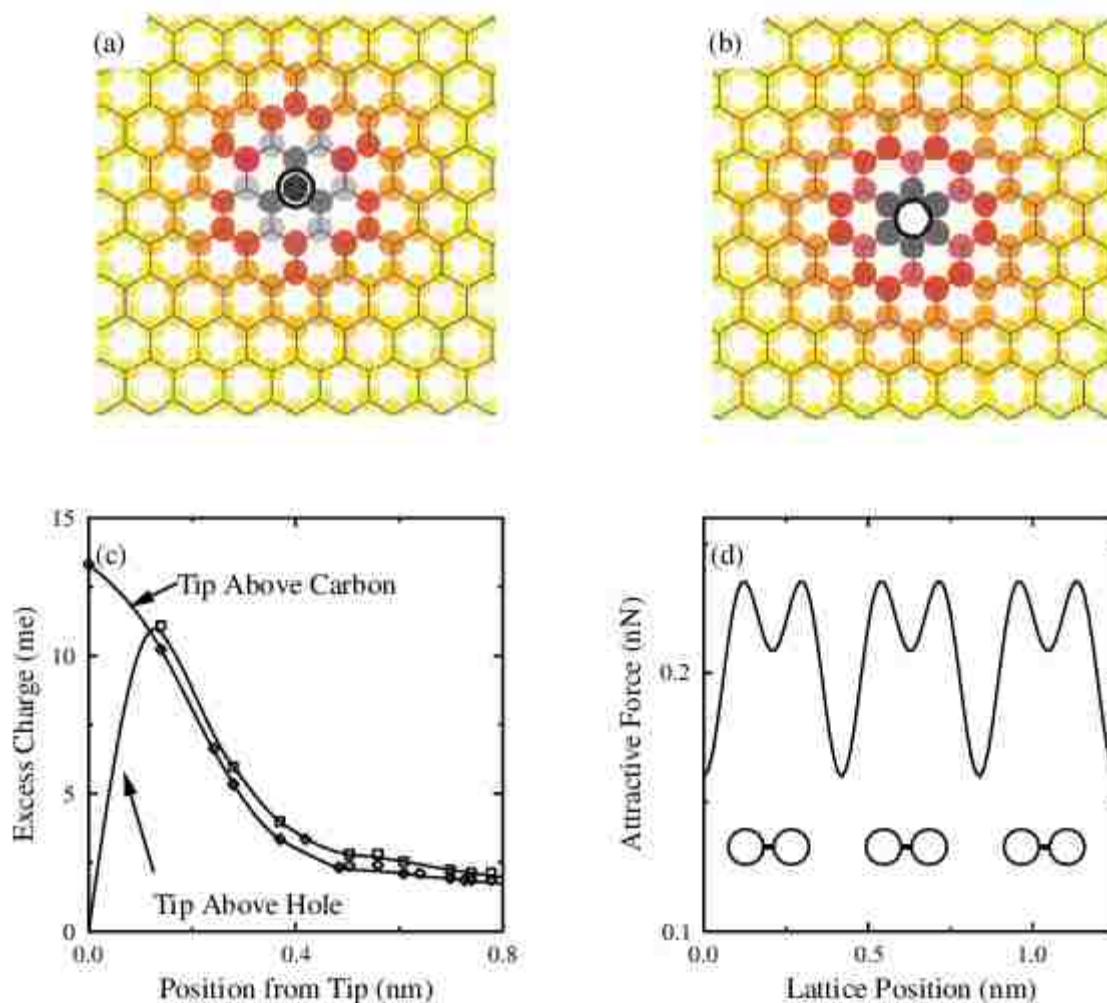
Figure 6: Summary of first-principles calculations performed with a unit charge held 0.1 nm above a 20 nm × 20 nm patch of graphene. (a) Topographic plot of charge density in the plane with the charge held directly above a carbon atom. (b) Topographic plot of charge density in the plane with the charge held directly above the hole of a benzene ring. (c) Excess charge in the plane as a function of radial distance from the point below the charge. The top line corresponds to the case where the charge is directly above a carbon atom and the lower line to the case where the charge is above a hole. (d) Force on a unit charge held 0.1 nm above the surface as it is moved parallel to the surface and along a line from the center of the honeycomb to the nearest carbon atom. A maximum force occurs over the carbon atom.

plots the excess charge in the plane as a function of radial distance from the point directly below the point charge. In the first case the induced charge is about 30% larger than in the second at a radial distance of zero, with the charge distributions in both cases becoming equivalent at a radial distance of about 0.5 nm.

The electrostatic force between the tip and the graphene due to this induced charge is plotted as a function of tip position relative to a honeycomb lattice in Fig. 6(d). In this case the position is along a line connecting a random carbon atom to its nearest neighbor. The force is unsurprisingly maximized directly above a carbon atom. It drops to about 80% of its max value between nearest neighbors and to about 60% of its max value when above a hole, oscillating perfectly with the atomic spacing. In addition to this information about the magnitude of the force, it was also found that when the charge was placed directly above a point halfway between a hole and an atom, a lateral component of the force was found to exist (not shown). This lateral component was approximately 10% of the vertical component. This lateral force will pull the sample in a horizontal direction during the STM imaging of a freestanding graphene sample, accounting for the horizontal distortion already noted in Fig. 5(b).

The STM image shown in Fig. 5(b) was collected under constant-current conditions, and therefore the feedback circuit will adjust the position of the STM tip in such a way that the tip-sample separation will be approximately constant throughout the scan. As seen in Fig. 6(d), when the tip begins moving over a carbon atom during the scan an attractive force will be induced and the freestanding graphene surface will be expected to move towards the tip. The feedback circuit will then cause the tip to retract. In addition to the attractive electrostatic force an oppositely directed restoring force will be induced in the graphene as it is pulled from its equilibrium position. In order to study this restoring force another set of calculations were

performed by collaborators. Given that the tip interacts with the membrane at a point, a small graphene supercell with 50 atoms, width $2L \approx 2$ nm, was generated and the center atom displaced vertically, leaving the corner atoms fixed. The central atom was gradually displaced an amount d, through a series of 0.03 nm increments, up to a maximum perpendicular displacement of 0.30 nm from the plane. At each displacement, the other atoms were allowed to relax to the energy minimum. The atomic relaxation was carried within the local density approximation to density functional theory (DFT) with projector augmented-wave potentials[72] as implemented in the plane-wave basis set VASP code[73]. The restoring elastic force was obtained from the Hellman-Feynmann theorem as the derivative of the energy data versus displacement and displayed in Fig. 7(a). The inset of Fig. 7(a) shows a schematic of the supercell in a side view. The strained model is shown in Fig. 7(b) in a tilted view. The linear fit shown for distortions with $d/L < 0.1$ produced a spring constant of about 20 nN per nm.

C. DISCUSSION

Looking back to the corrugation amplitudes of about 1 nm in Fig. 5(b), we obtain a $d/L = (1$ nm$)/(3.25$ μm$)\sim 0.0003$, well within the linear region. We are thus in a position to describe the enhanced corrugation observed in the STM image of freestanding graphene shown in Fig. 5(b). As the biased STM tip scans across the sample an attractive electrostatic force is induced between the tip and sample which oscillates with the same wavelength as the electronic DOS. This attractive force causes the lateral displacement of the graphene sheet which in turn induces an elastic restoring force in the sheet. When the tip moves over a hole in the honeycomb, the electrostatic force decreases and the restoring force causes the graphene to retract. Meanwhile, the feedback circuit of the STM maintains the separation between the tip and the graphene throughout the scan. Thus the line profile taken from the STM image in Fig. 5(b) consists of two
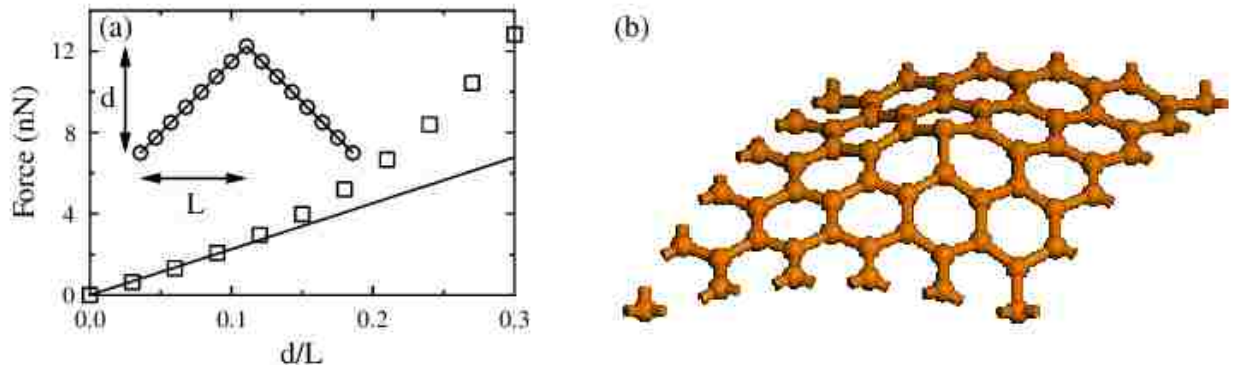
Figure 7: Results obtained from DFT calculations performed on a square graphene sheet of 50 carbon atoms and width $2L \approx 2$ nm. The corner atoms were pinned in place and the central atom lifted a vertical distance d in steps of 0.03 nm. (a) Restoring force of graphene calculated from DFT vs normalized displacement, with a linear fit completed over the range from 0 to 0.1. (b) Atomic model used in the DFT calculations shown in a tilted view.

parts,

$$d = d_{ind} + d_e, \tag{19}$$

where d_{ind} is the tip/graphene displacement caused by the net induced force in the graphene,

$$F_{ind} = F_{electrostatic} - F_{restoring}. \tag{20}$$

Since d_{ind} oscillates at the same wavelength as d_e, the net effect is that of enhanced corrugations with the same wavelength as those for a stationary graphene sample.

It is thus seen that an STM image of freestanding graphene will depend not only on the LDOS of the graphene surface but also on the electromechanical properties of the sheet. After the identification of the dynamic interaction between the STM tip and freestanding graphene attention was turned to how this interaction could be exploited. As discussed in detail in the following chapter, it is possible to perform constant-current STS experiments at a single point along the graphene sheet in which the tip height is measured as a function of tip bias. The data collected by the STM in these experiments gives us the displacement of the freestanding graphene due to the net induced force acting on the graphene sheet. Therefore if we could characterize the electrostatic force between the tip and graphene sheet as a function of tip bias we would also be able to characterize the restoring force in the sheet and thus measure elastic properties in the sheet. This effort will be described in the following chapter.

IV. ELECTROSTATIC MANIPULATION OF FREESTANDING GRAPHENE

When a voltage-biased tip is held near a grounded sample during an STM experiment the induced charge distribution in the area below the tip (and the resulting charge redistribution on the tip) will result in an electrostatic attraction between the two surfaces. This attraction is typically negligible when scanning surfaces that are tightly bound to the bulk material, but in the case of freestanding graphene there is no bulk and this interaction is expected to be significant. When the STM is in scan mode, the dynamic interplay between the electrostatic attraction and the elastic restoring force in the graphene results in enhanced corrugation in the STM image as shown in Fig. 5(b). The STM may also be used to perform single-point STS measurements on the freestanding graphene which can be used to probe the local electric and elastic properties of the sheet.

All succeeding STS measurements were taken during imaging and involve temporarily pausing the scan (such that no motion takes place parallel to the sample surface) while one of the tunneling parameters is varied. This chapter in particular deals with what will be referred to as $z(V)$ STS measurements. During these measurements the feedback circuit in the STM is left on and maintains a constant setpoint tunneling current while the tip bias is ramped from an initial to a final value, typically from 0.1 to 3 V. In this bias range the voltage is small enough for us to ignore field-emission effects[74,75]. The height of the tip (z) is then measured as a function of the tip bias. On a stationary sample this results in tip movements of ~ 1 nm due to the spatial variation in the LDOS as a function of energy. If the sample is capable of perpendicular motion, as in the case of freestanding graphene, then much larger movements are possible due to the sample deformation induced by the electrostatic attraction between the tip and sample discussed in the previous chapter. In the first section of this chapter I will present experimental $z(V)$

measurements with sample displacements on the order of tens of nanometers and will discuss the implications of such large displacements. In the following section I will present a model for estimating the electrostatic force between a biased STM tip and a grounded sample and use that model to convert the experimental $z(V)$ curves into more physically transparent force vs. displacement plots.

A. CONSTANT-CURRENT Z(V) STS MEASUREMENTS

Representative $z(V)$ measurements taken on a graphene on copper foil sample are shown in Fig. 8(a). The measurements were taken at set-point currents of 0.01, 0.1, and 1.0 nA respectively. In each of these measurements the tip bias was increased from an initial value of 0.1 V to a final value of 3 V. Each curve begins with a sharp increase with voltage followed by a region in which the height changes more slowly with the tip bias, with the difference in the two regions most pronounced in the 1.0 nA curve. The total tip displacement over this voltage range increases with the tunneling current. The total displacement in the 1.0 nA curve is about 2 nm, and the displacement for the 0.01 nA curve is about half of that. For comparison, identical $z(V)$ measurements were taken on a stationary gold substrate and are displayed in Fig. 8(b). In contrast to those taken on the graphene/Cu sample, these $z(V)$ curves do not appear to feature the two-region structure and current dependence seen in Fig. 8(a). However, the total displacements observed are comparable, and we take the curves on the graphene/Cu sample to be characteristic of the dependence of the tunneling probability changes with tip bias for pristine graphene. These curves will be referred to as $z_e(V)$.
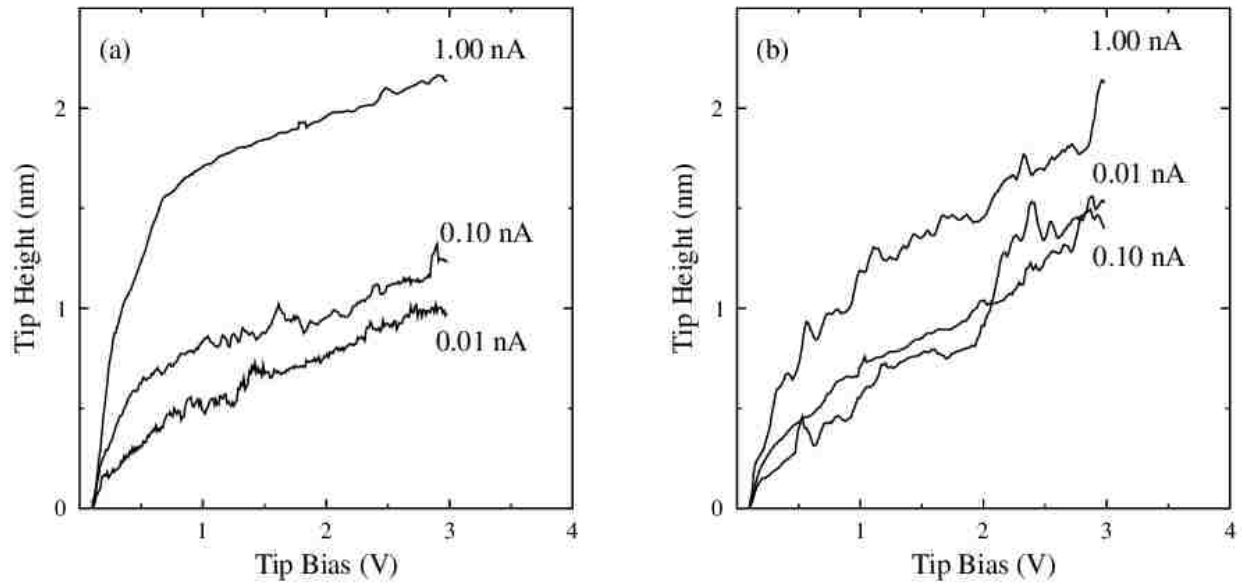
Figure 8: Constant-current $z_e(V)$ measurements showing the displacement of the STM tip as the tip bias voltage is ramped from 0.1 to 3.0 *V* for two different samples. Both data sets were collected with current setpoints of 0.01, 0.10, and 1.00 nA. (a) Data collected on a graphene on copper foil sample. (b) Data collected on a gold surface.

Representative $z(V)$ curves taken on a freestanding graphene sample (graphene on a TEM grid) with set-point currents of 0.01, 0.1, and 1.0 nA respectively are shown in Fig. 9. As with those taken on the graphene/Cu sample, these curves generally feature two regions (sharp increase with tip bias as well as plateaus), and the total displacement over the voltage range increases with the tunneling current. However, the total displacements in Fig. 9 range from about 5 to 30 nm, an order of magnitude larger than those for the stationary sample. The actual tunneling currents were simultaeously measured during each of these measurements and are plotted on a logscale in the inset. The tunneling current remained approximately constant (within a few percent) throughout each measurement, indicating that the graphene sheet must have been displaced along with the tip in these measurements. We can now write the relationship

$$z(V) = z_e(V) + z_g(V), \tag{21}$$

where $z(V)$ is the measured displacement of the tip, $z_g(V)$ is the displacement of the graphene sheet, and $z_e(V)/z_g(V) \approx 0.10$.

The displacement in the graphene sheet $z_g(V)$ is due to a mechanism similar to the one described in the previous chapter. As the tip bias is increased the electrostatic attraction between the tip and sample can be expected to increase as well. This will result in the graphene sheet moving towards the tip. This motion will result in a momentary decrease in the tip/graphene separation (s) and therefore an increase in the tunneling current. The feedback circuit is on during these measurements and will cause the tip to retract until the set-point current is reestablished. It is important to note that these measurements feature relatively small voltage steps of about 10 mV and long delay times (~ 3 ms) so that the data is recorded only after the tip/graphene/feedback circuit system has reached a new equilibrium. The net result is a large displacement of the graphene sheet as the tip bias is increased from 0.1 to 3 V.
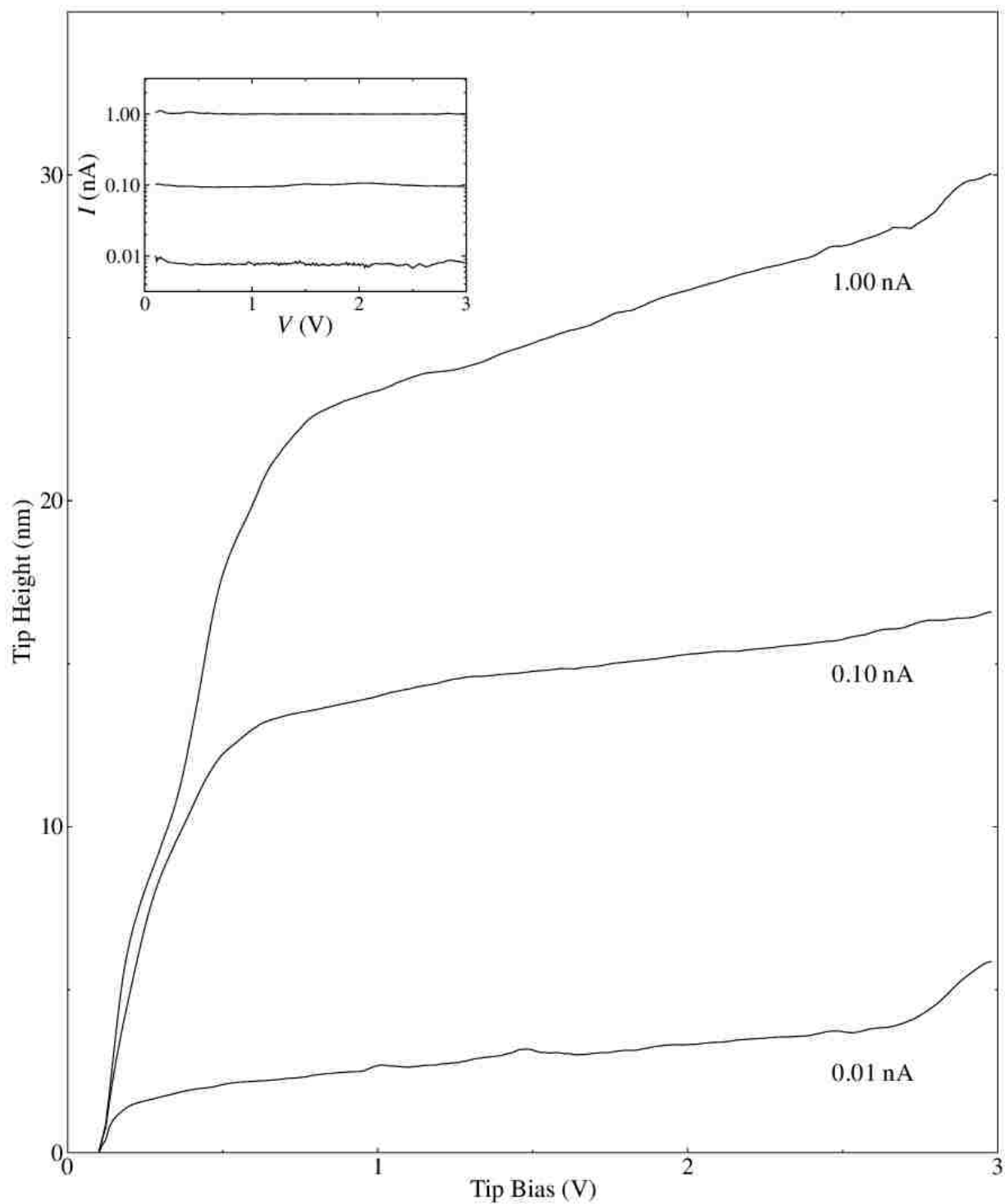
Figure 9: Constant-current $z(V)$ measurements showing the displacement of the STM tip as the tip bias voltage is ramped from 0.1 to 3.0 *V* taken on freestanding graphene. The measurements were taken with current setpoints of 0.01, 0.10, and 1.00 nA. The inset shows the measured current on a log scale as a function of tip bias during the corresponding $z(V)$ measurements.

The net force displacing the graphene sheet at each step is a sum of the oppositely directed electrostatic and elastic restoring forces (Eq. (20)). The electrostatic force is assumed to be a function of the tip bias V and the tip/graphene separation s,

$$F_{electrostatic} = F_{es}(V, s). \qquad (22)$$

At each data point along the $z(V)$ curve equilibrium between the electrostatic and restoring forces is established. Accordingly, if we could characterize $F_{es}(V, s)$ we would also know at each step the magnitude of the restoring force, and we could then infer information about the sheet's elastic properties. The remainder of this chapter will be occupied with the description of a model used to calculate the electrostatic force between the biased tip and grounded sample as a function of both V and s.

B. ELECTROSTATIC MODEL OF THE TIP-GRAPHENE SYSTEM

In order to calculate the force between a biased tip and grounded graphene sheet, a number of simplifying assumptions were made. The graphene sheet was modeled as a perfectly conducting surface. This approach is partially justified by the first principle tight-binding calculations reported in the third chapter of this dissertation and summarized in Fig. 6. Those calculations gave the charge distribution in a graphene sheet due to a point charge situated 0.1 nm above the sheet, and the induced charge distribution is similar to the solution for a point charge held above a perfectly conducting plane. The STM tip was modeled as a biased sphere. This not only gives the problem a convenient geometry, but is justified by numerous SEM studies of electrochemically etched tungsten atomic probes which reveal a spherical geometry at the tip of such probes. From these studies we can also estimate a tip radius of about 20 nm in our experiments[76].

Our problem is now framed as that of a biased conducting sphere held above a grounded conducting surface. We will use the label a for the radius of the sphere and V for the uniform potential the sphere experiences. For simplicity's sake, we will start by solving the problem in the case where the grounded surface is an infinite plane, as shown with relevant parameters in Fig. 10. The distance between the bottom of the sphere and the plane is labelled s and the grounded plane defines the $z = 0$ plane, so that the center of the sphere is located at

$$z_0 = s + a. \tag{23}$$

The potential above the plane and outside the sphere must satisfy Laplace's equation

$$\nabla^2 \Phi = 0 \tag{24}$$

and meet the two boundary conditions

$$\Phi = 0, z = 0 \tag{25}$$

and

$$\Phi = V, x^2 + y^2 + (z - z_0)^2 = a^2. \tag{26}$$

This electrostatic problem can be solved with arbitrary accuracy through the method of images[77,78]. This method generates an auxilliary problem in which the physical surfaces are no longer present but in which two or more image charges are arranged in such a way that the appropriate boundary conditions are still met. As long as the image charges are not placed in the space where the solution is sought, a uniqueness theorem guarantees that two solutions to Laplace's equation with identical boundary conditions are in fact the same solution. Thus the solution to the auxilliary problem is the solution to the original problem. We will therefore momentarily ignore the spherical and plane conductors and contemplate a series of charges being placed along the z-axis.

Figure 10: Model of the biased STM tip/grounded graphene system. The tip is modeled as a conducting sphere at potential *V*. The graphene is modeled as a grounded infinite conducting plane. These two surfaces define the two boundaries of the resulting electrostatic problem. The distance between the plane and the nearest point on the sphere is labelled *s* and the radius of the sphere is labelled *a*. The center of the sphere is then located at $z_0 = s + a$.

A point charge of magnitude

$$q_0 = 4\pi\epsilon_0 aV = \frac{aV}{k} \tag{27}$$

located at $z = z_0$ will satisfy the spherical boundary condition but not the planar one. An image charge, that is a point charge of magnitude $-q_0$ located at $z = -z_0$, will result in the planar boundary condition being met, but the spherical one will no longer be satisfied. We might suppose that a second charge can be placed in the $z > 0$ half-space with a magnitude and position such that the spherical boundary is satisfied again. We now seek a q_1 and z_1 such that, for instance, the following two equations,

$$\frac{q_0}{a} - \frac{q_0}{2z_0 + a} + \frac{q_1}{(z_0 + a) - z_1} = 0 \tag{28}$$

and

$$\frac{q_0}{a} - \frac{q_0}{2z_0 - a} + \frac{q_1}{(z_0 - a) - z_1} = 0 \tag{29}$$

are met. The simultaneous solutions to these equations are

$$\bar{q}_1 = \frac{q_1}{q_0} = \frac{a}{2z_0} \quad z_1 = z_0 - \frac{a^2}{2z_0}. \tag{30}$$

There are two key points here. The first is that $a < z_0$ and therefore $a^2/2z_0 < a$ and q_1 will lie inside the spherical boundary. The second is that $q_1/q_0 \approx 0.5$ and we might expect successive sets of image charges to continuously decrease in magnitude. Repeating the above prescription yields a series of sets of image charges defined by the iterative relationships

$$\bar{q}_n = \frac{q_n}{q_0} = \frac{a\bar{q}_{n-1}}{z_0 + z_{n-1}} \tag{31}$$

and

$$z_n = z_0 - \frac{a^2}{z_0 + z_{n-1}}, \tag{32}$$

39

where q_0 and z_0 were defined in Eq. (27) and Eq. (23) respectively. The potential in the region $z > 0$ and outside the spherical boundary is then

$$\Phi(\boldsymbol{r}) = \sum_{n=0}^{\infty} \frac{kq_n}{|\boldsymbol{r} - \boldsymbol{z_n}|} + \frac{-kq_n}{|\boldsymbol{r} + \boldsymbol{z_n}|} \tag{33}$$

$$= aV \sum_{n=0}^{\infty} \left[\frac{\bar{q}_n}{\sqrt{x^2 + y^2 + (z - z_n)^2}} - \frac{\bar{q}_n}{\sqrt{x^2 + y^2 + (z + z_n)^2}} \right].$$

As noted above, $a < z_0$, as long as $s \neq 0$, and therefore it is evident that the charges in the upper half-space will remain in the spherical boundary and thus Laplace's equation will be satisfied by this potential. I will show below that the boundary conditions (25) and (26) are satisfied when considering only a finite number of terms.

Once the image charge magnitudes and locations are known we may discard the auxilliary problem and return again to the problem outlined in Fig. 10. The total charge induced on the sphere is Q, where

$$Q = \sum_{n=0}^{\infty} q_n = \frac{aV}{k} \sum_{n=0}^{\infty} \bar{q}_n, \tag{34}$$

and the total charge induced on the plane is $-Q$. Recalling that the plane is grounded while the sphere is an equipotential, the electrostatic energy of this system is

$$U = \frac{1}{2} QV = \frac{aV^2}{2k} \sum_{n=0}^{\infty} \bar{q}_n. \tag{35}$$

The electrostatic force between the sphere and plane is

$$F = -\nabla U = -\frac{aV^2}{2k} \sum_{n=1}^{\infty} \frac{d\bar{q}_n}{dz_0} = -\frac{aV^2}{k} \sum_{n=1}^{\infty} \bar{q}_n' \tag{36}$$

The derivative that apears in Eq. (36) can be evalated using the iterative relationships

$$\bar{q}'_n = \frac{a\bar{q}'_{n-1}}{z_0 + z_{n-1}} - \frac{a\bar{q}_{n-1}}{z_0 + z_{n-1}} \frac{(1 + z'_{n-1})}{z_0 + z_{n-1}} \tag{37}$$

and

$$z'_n = 1 + \frac{a^2}{z_0 + z_{n-1}} \frac{(1 + z'_{n-1})}{z_0 + z_{n-1}}, \tag{38}$$

with $\bar{q}'_0 = 0$ and $z'_0 = 1$. These formulas and others not discussed here, such as those describing the electric field in the half-space and charge distribution on the plane, are summarized in Appendix A of this dissertation.

The four iterative sets of quantities $\bar{q}_n$, $\bar{q}'_n$, z_n, and z'_n were evaluated in *Mathematica*. It was critical to first determine the asymptotic values of $\bar{q}_n$ and $\bar{q}'_n$ as $n \to \infty$ because the sums in Eqs. (33) and (36) would need to be estimated based on a finite number of terms. The quantities $\bar{q}_n$ and $\bar{q}'_n$ depend only on the ratio $a/z_0 = (1 + s/a)^{-1}$. SEM studies of electrochemically etched STM tips place a lower limit on a of 20 nm. While the exact value s is not known, a conservative estimate would assign it a value of 0.5 nm. Using these values for the parameters, the values of $\bar{q}_n$, $\bar{q}'_n$, z_n, and z'_n were calculated using the code found in Appendix B up to $n = 1000$ and plotted in Fig. 11. These plots reveal that $\bar{q}_n$ and $\bar{q}'_n$ decrease to zero, and that as expected the z_n lie within the spherical boundary. After 150 iterations, both $\bar{q}_n$ and $\bar{q}'_n$ are found to be at least 10^{-10} times their max values. All further sums will be performed by truncating the infinite sums after the $n = 150$ term.
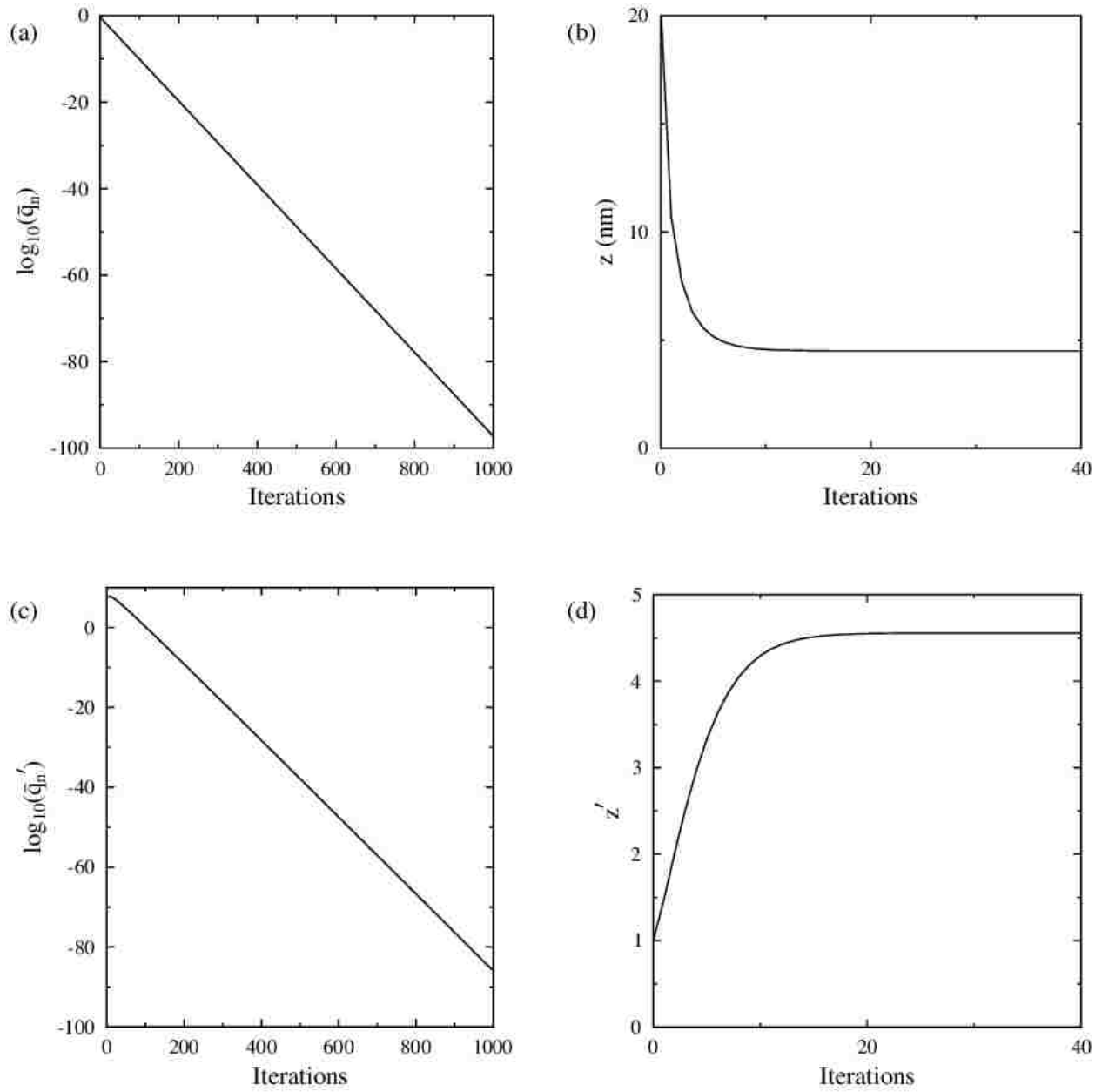
Figure 11: Iterative quantities generated by the image solution and plotted against iteration number. (a) Log plot of the normalized image charge magnitude. The exponent of the charge magnitude decreases linearly with the number of iterations. (b) Locations of image charges on the z axis as a function of iteration number. The asymptotic is 4.5 nm, within the spherical boundary at $z = 0.5$ nm. (c) Log plot of the image charge derivative used in calculating the electrostatic attraction. It decreases similarly to the image charge magnitude. (d) The position derivatives used in calculating the force.

I next confirmed that the boundary conditions (25) and (26) had been met. *Mathematica* code yielding the potential at some point $r = (x, y, z)$ can be found in Appendix B. In order to confirm the boundary condition on the plane I evaluated the potential, using the standard values for a and s and unit bias, at $z = 0$ at 500 points along the Archimedean curve defined by the parametric equations

$$x = s\theta \cos\theta \quad y = s\theta \sin\theta \tag{39}$$

where θ was increased in equal steps from 0 to $10 * 2\pi$. A plot of the curve on the plane can be found in Fig. 12(a). *Mathematica* returned a value of $\Phi = 0$, within floating-point precision, at every point along the curve, confirming that the boundary condition (25) was met. In order to confirm the boundary condition on the sphere I evaluated the potential, using the standard values for a and s and unit bias, at 500 points along the spherical curve defined by the parametric equations

$$x = \frac{a \cos\theta}{\sqrt{1 + 0.1\theta^2}} \quad y = \frac{a \sin\theta}{\sqrt{1 + 0.1\theta^2}} \quad z = -\frac{as\theta}{\sqrt{1 + 0.1\theta^2}} \tag{40}$$

where θ was increased in equal steps from $-10 * 2\pi$ to $10 * 2\pi$. A plot of the curve on the sphere can be found in Fig. 12(b). *Mathematica* returned a value of $\Phi = 1$, within floating-point precision, at every point along the curve, confirming that the boundary condition (26) was also met. With the validity of the solution confirmed I will now use this model to calculate the attractive electrostatic force between the STM tip and grounded graphene sample in the experimental $z(V)$ curves introduced above and shown in Fig. 10.

C. EVALUATION OF THE ELECTROSTATIC FORCE IN THE STS Z(V) CURVES

Single point evaluations of the electrostatic force described by Eq. (36) depend on three parameters, a, s, and V. It is reasonable to assume that a remains constant throughout these
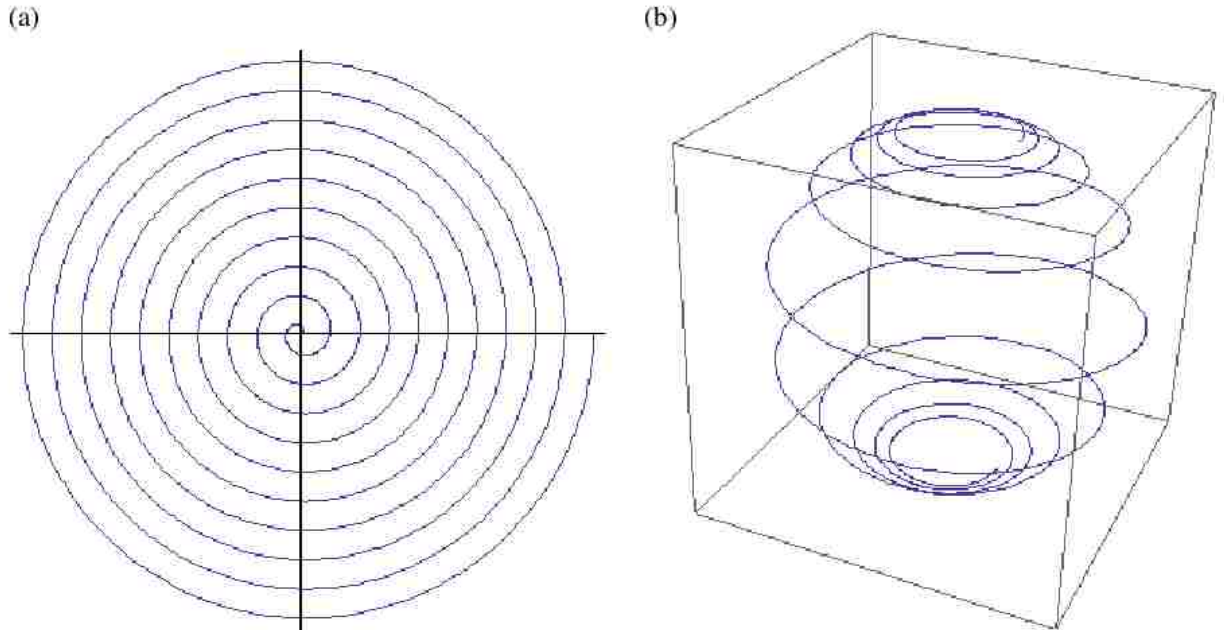
43

Figure 12: Curves along which the boundary values of the potential (33) were measured with standard parameters and unit sphere bias. (a) The planar boundary was tested along the Archimedean curve described by Eq. (39). The correct value of $\Phi = 0$ was found everywhere within floating-point precision. (b) The spherical boundary was evaluated using the spherical spiral described by Eq. (40). The correct value of $\Phi = 1$ was found everywhere within floating-point precision.

measurements, and V is the independent variable controlled by the STM during the measurements. The tip-graphene separation s, however, is neither constant nor controlled. We know from the measurements in Fig. 8 that this parameter varies with tip bias due to variation in the tunneling probability, and therefore it is proper to write

$$s = s_0 + s(V) \tag{41}$$

where s_0 is the initial separation. The varying part of this sum $s(V)$ is determined by the measurements taken on a stationary sample shown in Fig. 8, but the initial separation cannot be measured by our STM. However, basic STM theory tells us that a value of $s_0 = 0.5$ nm is a reasonable value, and that is the value I will use for all subsequent calculations. Because s varies with the tip bias, the image charge magnitudes and locations will also vary with the bias. This means that the electrostatic force $F(V)$ described in Eq. (36) will not have the simple quadratic form suggested by that equation, but instead will have some complicated form which I will explore numerically.

I will begin by rewriting Eq. (36) in the form

$$F = \frac{aV^2}{k} \bar{Q}'(a, s) \tag{42}$$

where

$$\bar{Q}' \simeq \sum_{n=1}^{N} \bar{q}'_n[a, s(V)]. \tag{43}$$

Because a is assumed to be constant in these measurements, I numerically evaluated the sum (43) in *Mathematica* for constant a and varying s. Details of this evaluation and the code used can be found in Appendix C. The resulting curves were closely fitted with power functions, and for the standard parameter value $a = 20$ nm, it was found that

$$\bar{Q}'(s) = 0.1264 * s^{-1.061}. \tag{44}$$

45

The experimental $s(V)$ curves in Fig. 8 were given polynomial fits (see Appendix C) so that the electrostatic force (42) could be expressed as a function solely of the parameters a and I and the independent variable V. The resulting $F(V)$ curves, with $a = 20$ nm and $I = 0.01, 0.1,$ and 1.0 nA, are plotted from $V = 0$ to $V = 3$ in Fig. 13.

We treat the experimental $z(V)$ curves shown in Fig. 9 as quasistatic measurements. These measurements are fully reversible and are not altered when that time delay between the voltage step and measurement is increased. If the graphene-tip-feedback circuit system is indeed at equilibrium when the z measurements are recorded, then the above analysis combined with the experimental measurements can yield information regarding the elastic properties of the graphene sheet. Towards this aim the theoretical $F(V)$ curves were used along with the experimental $s(V)$ curves to convert the $z(V)$ measurements into $F(d)$ where d is the displacement of the graphene alone,

$$d = z - s. \tag{46}$$

Example $F(d)$ plots, taken from the $z(V)$ data presented in Fig. 9, are shown in Fig. 14 for tunneling currents of 0.01, 0.1, and 1.0 nA. These $F(d)$ plots allow for the direct measurement of both the spring constant associated with the motion along with the energy required to displace the sheet that distance.

D. DISCUSSION

There are two key aspects of the $F(d)$ plots shown in Fig. 14 to discuss. The first is that the electrostatic force is on the order of a few nano-Newtons at the higher biases. This would put the electrostatic force between the tip and the sample in competition with attractive London-van der Walls dispersion forces between small (~ 3 nm) neutral nanoparticles and a graphene sheet, which would be estimated to be approximately 0.1 nano-Newtons according to Hamaker
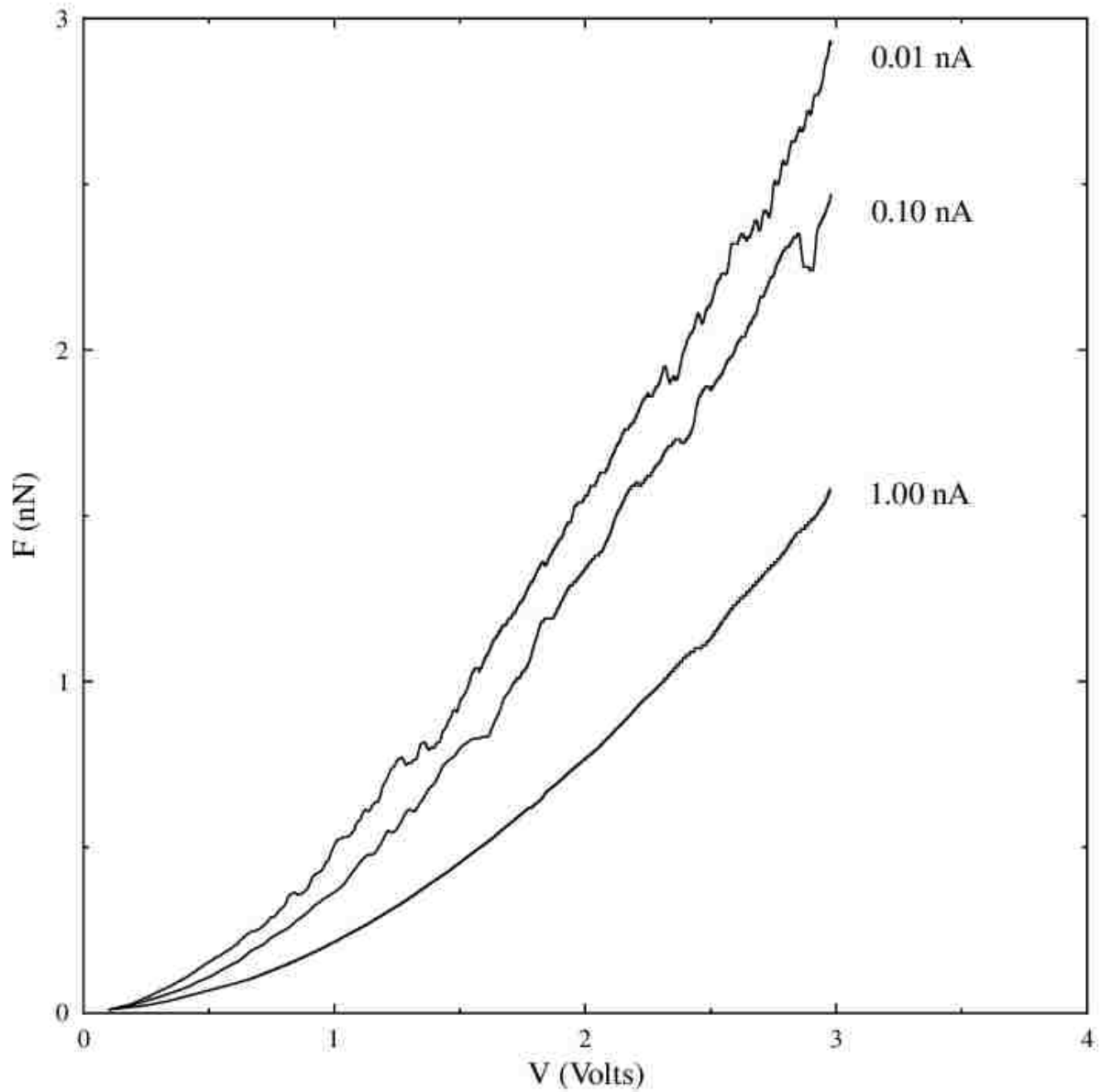
Figure 13: Theoretical *F(V)* curves for freestanding graphene generated using Eqs (42) and (44) in conjunction with the experimental *s(V)* curves for current setpoint values of *I* = 0.01 nA, 0.10 nA, and 1.00 nA. The smallest tunneling current requires the smallest tip-graphene separation, and therefore the largest tip-graphene attraction.
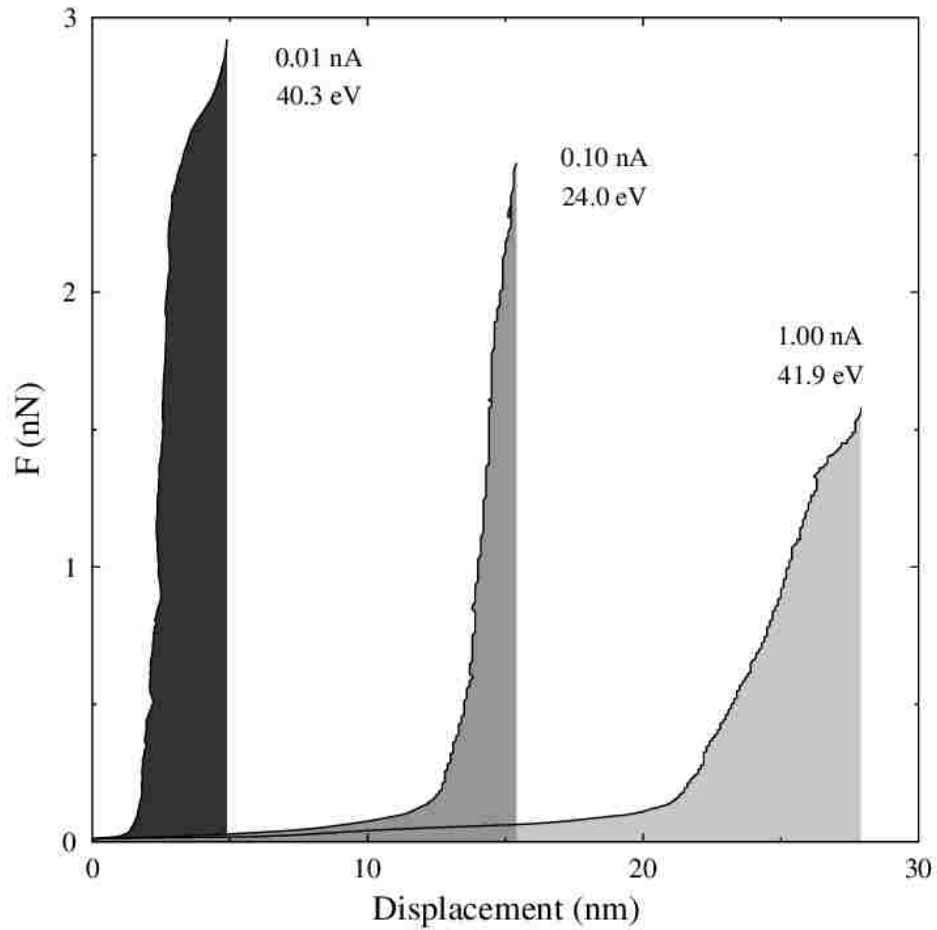
Figure 14: Force-displacement curves for freestanding generated by the experimental *z(V)* curves shown in Fig. 9 and the theoretical *F(V)* curves in Fig. 13 for current setpoint values of *I* = 0.01 nA, 0.10 nA, and 1.00 nA.. The displacement of the graphene sheet was found using Eq. (46). The area underneath each curve yields the work done by the tip in displacing the graphene sheet.

theory[79]. The second is that there appear to be two regions in the plot for all three current setpoints. Initially the force changes slowly with displacement. As already noted, it is well known that the surface of the freestanding graphene is covered in ripples of small amplitude (~0.5 nm) and relatively long wavelength (~ 10 nm)[12,35]. Therefore there is excess graphene compared to a sheet which was perfectly flat, and this initial region possibly corresponds to the force required to remove those ripples. Afterwards, further displacement of the sheet will require stretching the very strong in-plane carbon-carbon bonds in the graphene sheet, corresponding to the second region in which the electrostatic force increases sharply with displacement.

In conclusion, a novel STM technique has been developed which measures local elastic properties in flexible materials. An image charge model was used to generate Force-displacement plots from the experimental $z(V)$ data. This technique can be used to directly measure changes in the local electromechanical properties of freestanding graphene due to local defects or functional groups, as demonstrated in the following chapter.

V. SELF-ORGANIZED PLATINUM NANOPARTICLES ON FREESTANDING GRAPHENE

Direct methanol and ethanol fuel cells are excellent power sources due to their high energy density, low pollutant emission, low operating temperature, and the ease of handling liquid fuel[84]. In these devices, oxygen is reduced at the cathode while the fuel is oxidized at the anode. Catalysis is critical to both of these reaction sequences, and the most popular candidate for catalyzing both reduction and oxidation is the noble metal platinum (Pt). However, the worldwide supply of Pt is inadequate for mass production. In response, researchers have moved toward increasing the Pt surface-area-to-volume ratio through the use of nanoparticles (NPs). Platinum NPs 2 nm to 5 nm in size, and even as small as 0.9 nm, can be used to replace a solid Pt film without losing catalytic activity due to quantum size effects[85,86]. Among the most effective supports for Pt NPs in electrochemical catalysis are carbon materials due to their large surface areas for dispersion of the NPs, a porous structure for transferring reactants and products, and good electrical conductivity for electrochemical reactions[87,88]. In particular, graphene appears to be the ideal support for Pt NP catalysis, with its unmatched electrical conductivity, strength, and surface-to-volume ratio[89,90]. Furthermore, some theoretical studies have predicted that by placing certain elements on graphene the catalytic reactions are enhanced[91].

First-principles studies using Pt NPs have shown that the binding between an NP and a graphene sheet strongly depends on the number of Pt atoms and their geometry[92]. For example, as the number of Pt atoms in the NP increases, the Pt-C interaction energy per contacting Pt atom decreases, which results in fewer planar NPs and more 3D clusters[93]. Furthermore, temperature affects the morphology of suspended graphene, the adsorption process, and binding energy[94], making this a difficult system to model without experimental data for

50

comparison. In an effort to better understand this complicated system, we collected both STM

and STS data on a Pt NP functionalized freestanding graphene sheet. Coupled with TEM images

and molecular dynamics simulations, a complete description of the Pt NP/graphene system at the

atomic scale was formed.

A. SAMPLE DESCRIPTION AND CHARACTERIZATION

The freestanding graphene samples used in this study were identical to those described in the

third chapter of this dissertation. Pt NPs were grown on the freestanding graphene using a single-

step sputtering process, in which argon ions (Ar+) bombarded a Pt target and the ejected Pt

atoms were allowed to land on the membrane, as illustrated in Fig. 15a. Bright-field TEM images

of the Pt NPs supported by freestanding graphene are displayed in Figures 15b - d.

Approximately 2,000 NPs, seen as minute black points, are uniformly dispersed on the 170 nm $\times$

170 nm area shown in Fig. 15b. Zooming in, the 30 nm $\times$ 30 nm image shown in Fig. 15c reveals

that the NPs prefer a specific nearest-neighbor distance, tend to line up, and have a number

density of 6.6×10^{12} cm^{-2}. Analysis of all 70 Pt NPs in this view reveals that more than 50%

show a clear and similar crystal structure. Zooming further still, a 10 nm $\times$ 10 nm image

displayed in Fig. 15d shows the highest magnification obtained, at which point the atomic-scale

details of the NPs can be clearly seen. The measured inter-planar spacing of 0.20 nm and 0.23

nm (marked on Fig. 15d) corresponds to those of (200) and (111) planes, respectively, in a Pt

single crystal. Fast Fourier transform analysis shows that the zone axis of these NPs is along the

$[01\bar{1}]$ direction. A size analysis of the particles is presented in the histogram in Fig. 15e,

showing a narrow size distribution with an average diameter of 1.4 nm $\pm$ 0.2 nm.
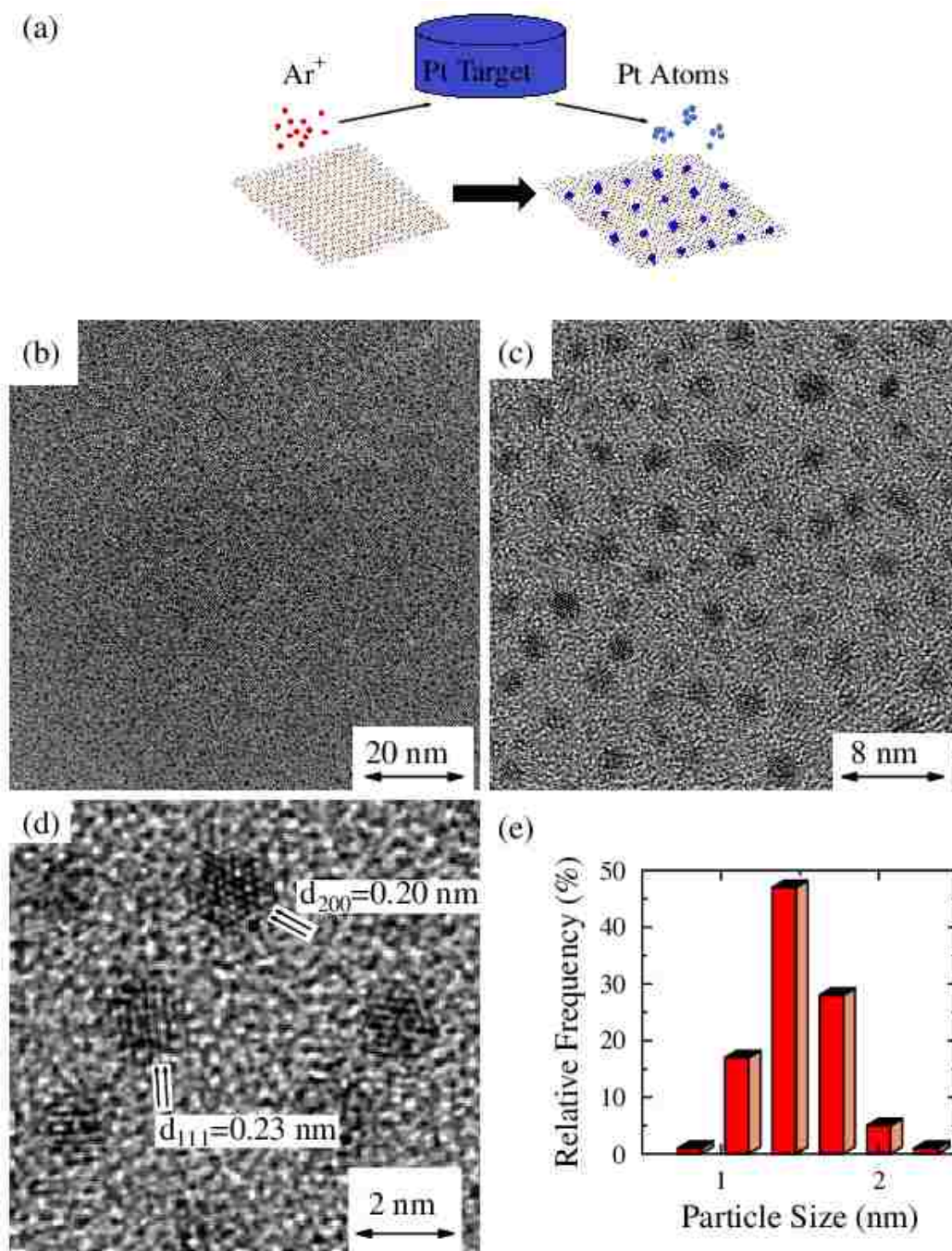
Figure 15: Synthesis and characterization of the Pt NP functionalized graphene. (a) Schematic showing the single-step sputtering process for deposition of Pt onto a freestanding graphene membrane. (b – d) HRTEM images of Pt NPs supported by a freestanding graphene membrane with three different magnifications. Atomic-scale features, including the distances between atomic planes, can be resolved in (d). (e) Histogram showing particle size.

To decipher the periodicity of the NP arrangement observed in Fig. 15c, the autocorrelation function (ACF) of that image was calculated and is displayed in Fig. 16a. The overall symmetry is not very well defined, but it does slightly favor the honeycomb symmetry of the graphene lattice. A line profile taken from the ACF along the drawn diagonal line is shown in Fig. 16b. From this, the average particle size, as determined by the distance at $1/e$ of the initial peak, is found to be about 1.3 nm, consistent with the results of the size analysis reported above. The presence of the second peak in the line profile confirms ordering in that direction, while its location of 4 nm is the preferred nearest-neighbor separation of the NPs.

To learn about the height and the top surface topography of the Pt NPs, atomic-scale STM images were obtained. A typical filled-state, 12 nm $\times$ 12 nm STM image is shown in Fig. 17a, revealing an artificially stretched honeycomb lattice near a pair of large white features (indicating increased height). A white box marks the original location of the lower right inset and highlights the stretched honeycomb lattice, while the left inset was acquired far from the NPs and shows the normal lattice constant. The large white shapes in Fig. 17a are determined to be Pt NPs based on the number density and average size observed in this and other STM images, combined with the TEM data showing the same details throughout the surface. Vertical and horizontal line profiles, running through the center of Fig. 17a along the lines shown in red and blue, were extracted from the image. The horizontal line profile is plotted in blue directly below the image, while the vertical line profile is plotted in red at the bottom. A large peak corresponding to the central NP appears in both curves. In the horizontal profile, moving from left to right, we find that the tip height increases approximately 0.6 nm to the top of the NP and decreases 1 nm to the base, while in the vertical profile it increases 1.2 nm to the top and
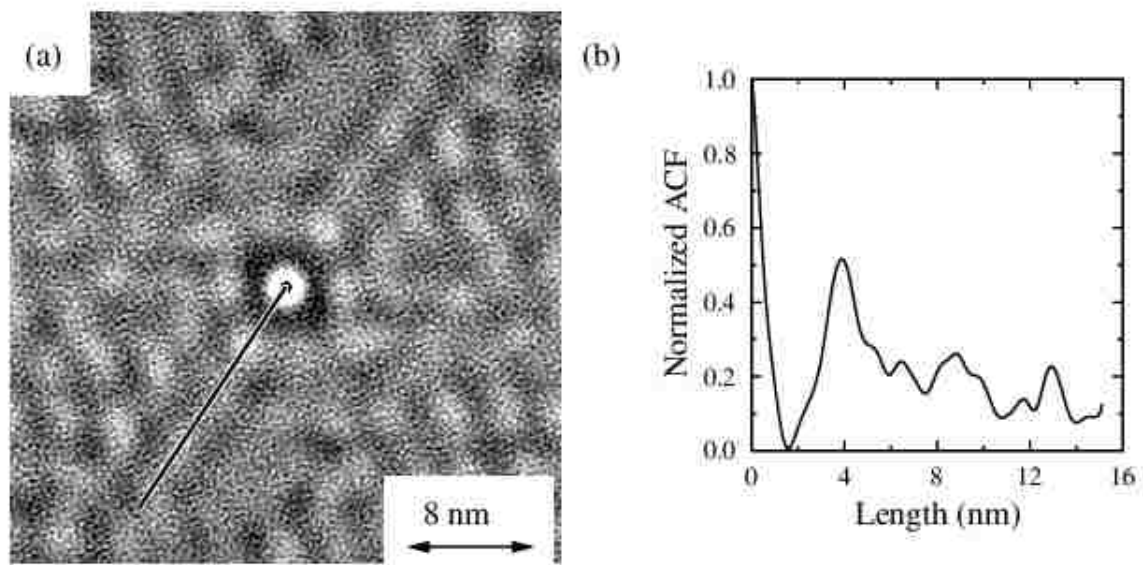
Figure 16: (a) The ACF of the image in Fig 15c. (b) A line profile taken along the line in part (a) and used to find an average particle size and nearest-neighbor distance.
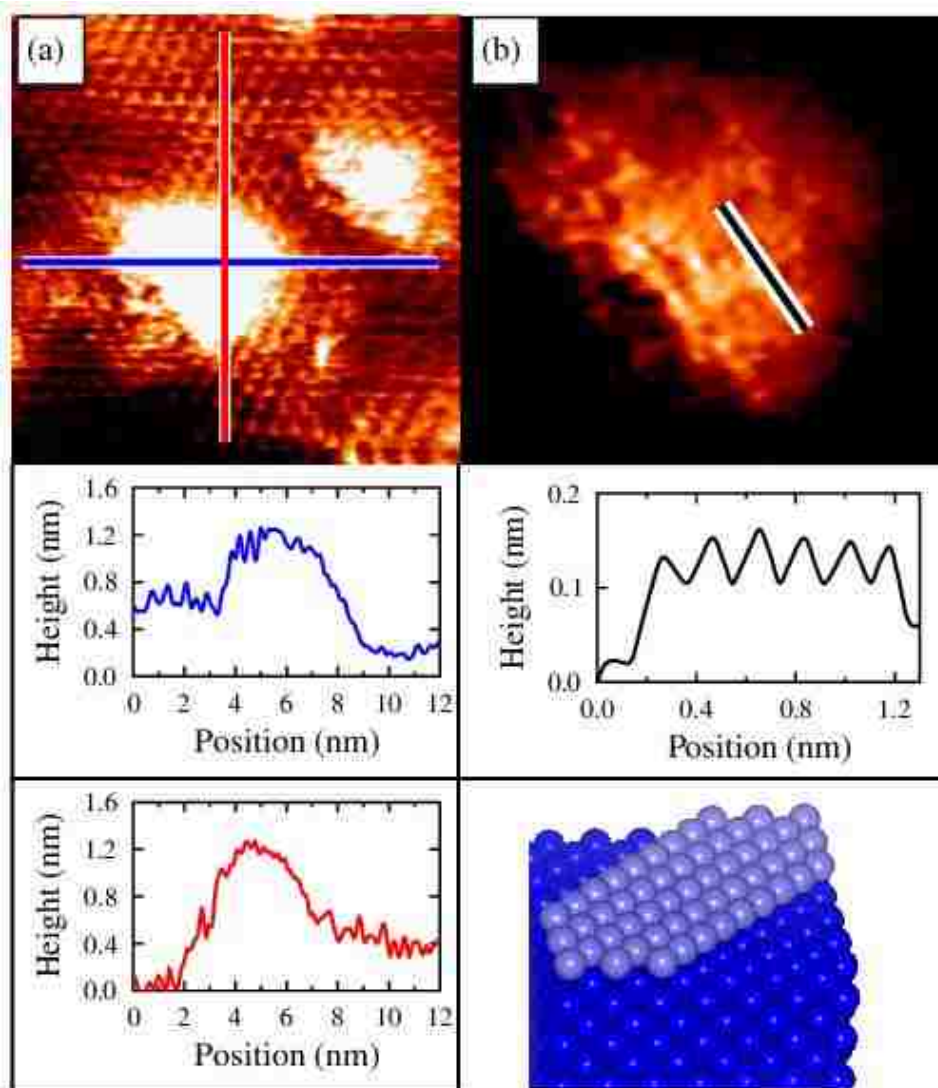
Figure 17: (a) 12 nm × 12 nm filled-state STM image of Pt NPs on suspended graphene. The lines mark the locations where the line profiles were obtained. The horizontal line profile is plotted in blue directly below the image, and the vertical line profile is plotted in red below the first graph. Both show the height profile for the same NP. The lower left inset image is pristine graphene acquired further away from the NPs. The lower right inset image shows the artificially enlarged graphene at the spot marked by the white box. Both inset images are magnified and measure 1.2 nm by 1.2 nm. (b) Cropped image of the larger NP in part (a), displayed with a compressed color scale to show the atomic rows. A line profile was taken near the line shown and is plotted directly below the image. Below that graph is a model of the Pt $(01\bar{1})$-oriented surface with the top layer highlighted.

decreases 0.8 nm to the base. The different height changes from one side to the other suggest that the local morphology of graphene is affected by the presence of the Pt NP. Note, the NP widths from the STM line profiles are affected by tip-sample convolution effects[95], but we can rely on the TEM data for that information. From the TEM data the width of the nanoparticles is about 1.4 nm, and this is larger than its height (from the STM data), indicating a preference for wetting the surface over 3D growth. Furthermore, we can conclude that only 2–3 layers of Pt atoms are present in this particular NP (i.e., Pt lattice constant = 0.39 nm).

Atomic-scale details on the surface of the Pt NP can be observed after a 5 nm × 5 nm area was cropped from Fig. 17a and given a compressed color scale to enhance the details as shown in Fig. 17b. We are able to faintly resolve atomic rows, which can be seen running diagonally from the lower left to the upper right. A local height line profile extracted along the overlaid line in Fig. 17b, shows the details better and is plotted just below the image. Clear oscillations occur with a small height corrugation of only 0.05 nm. The row-like symmetry of the surface topography is inconsistent with the honeycomb structure of graphene but is consistent with exposed Pt. The average distance between individual peaks (i.e., the individual rows) is ~0.20 nm, which matches the distance between the rows of atoms shown in the TEM image of Fig. 15d and suggests we have a $(01\bar{1})$-oriented surface with (200)-oriented planes. A simple drawing of a Pt structure having a $(01\bar{1})$-oriented surface is shown below the line profile. The surface has five rows of Pt atoms (highlighted) running from the lower left to the upper right. All totaled, we can confirm that the Pt NPs are securely affixed to the suspended graphene, as they are stable enough to be imaged with the STM, and that the graphene does not wrap around the NP. This is in contrast to systems where graphene encapsulation has been observed for nanocrystals[96] and bacteria[97].

In order to better understand the adsorption mechanism, we had collaborators carry out MD simulations using reactive force fields. We considered a square-shaped graphene with a computational unit cell of 12 nm × 12 nm which contains 8640 carbon atoms. Pt atoms were placed on the graphene sheet, initially arranged in a square lattice of lattice constant 0.3 nm and with a height of 0.34 nm, as shown in Fig. 18a. After MD relaxation (~1 ns) at low temperature (10 K), a new self-assembled structure had developed and is shown from three different viewpoints in Fig. 18b. The Pt atoms form an NP with no well-defined shape but having a lateral width of about 3 nm and a height of 0.5 nm, in quantitative agreement with our experimental results shown in Fig. 17. The important discovery here is that one atomic layer of Pt atoms over graphene is energetically unfavorable even at very low temperature, while condensing the NP decreases the total energy of the system. In addition, we found that competition between interatomic forces (i.e., between Pt-Pt and Pt-C atoms), limits the vertical growth to 2–3 layers of Pt atoms. The radial distribution function for Pt atoms in the NP of Fig. 18b revealed that almost all nearest neighbor Pt-Pt bonds were 0.278 nm long, and the lattice structure was a compacted structure different from perfect face-centered cubic (fcc). Interestingly, the NP is on average elevated above the substrate, with very few Pt atoms bonded to the graphene sheet, as evidenced by the right inset of Fig. 18b. The Pt-C bonds, which are mostly 0.2 nm long, are covalent in nature and ensure the stability of the NP on the surface up to room temperature, though it detached from the surface beyond that. Additional calculations and simulations were performed to test the Pt NP number density and crystallinity observed with TEM. Here, when five NPs with pre-imposed fcc structure are spaced apart from each other and

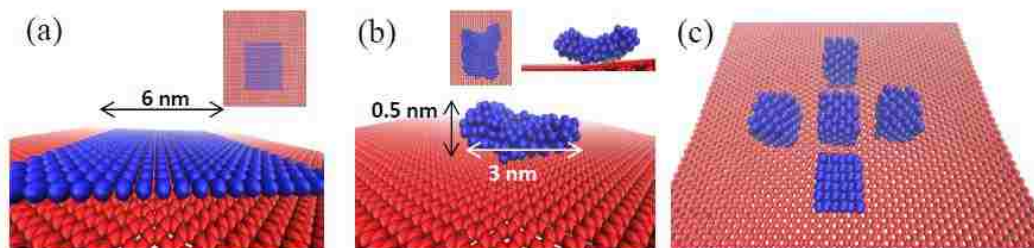*Figure 18:* (a) The initial arrangement of the Pt atoms over graphene in an MD simulation. (b) The final self-assembled structure after relaxation by MD computations at $T = 10$ K. A Pt NP was formed with a lateral size of 3 nm and height of 0.5 nm. The right (left) inset shows the side (top) view. (c) Five Pt NPs which were found to be stable at room temperature after a long MD simulation time when placed on the graphene surface.

allowed to relax at 300 K, they are stable, as shown in Fig. 18c. This confirms the viability of the

NP arrangement seen in Fig. 2, assuming thermal fluctuations in the graphene sheet remain

small. These NPs are found to sit on top of the graphene surface, and Pt atoms do not flow from

one NP to the other. In fact, the fcc NPs themselves maintained their structure even up to 1000

K.

In order to experimentally probe the strong binding between the Pt NPs and the graphene

sheet, we turned to the $z(V)$ STS measurement technique described in detail in Chapter 4. This

measurement was performed using a current setpoint of 1.00 nA, and typical results are

displayed in Fig. 19a. For comparison, the result for an inflexible control Au sample showing

almost zero displacement is shown on the bottom curve. The middle curve is what we measure

for pristine freestanding graphene and shows a net displacement of about 30 nm. The top curve is

what we measure for Pt-functionalized freestanding graphene, showing a net displacement of

about 140 nm. The enhanced displacement in the Pt-functionalized sample indicates that the

presence of the NPs has significantly changed the local electromechanical properties in the

graphene sheet. We have already determined that the graphene is not encapsulating the

nanoparticles, so these results cannot be explained by excess graphene being pulled away from

the NPs as the $z(V)$ measurement is made. Instead, it is likely this increased displacement is due

instead to a change in the local geometry in a graphene sheet near a Pt NP due to the covalent

bonds predicted to form between the NP and some carbon atoms, which will be expected to

affect the local restoring force in the sheet.
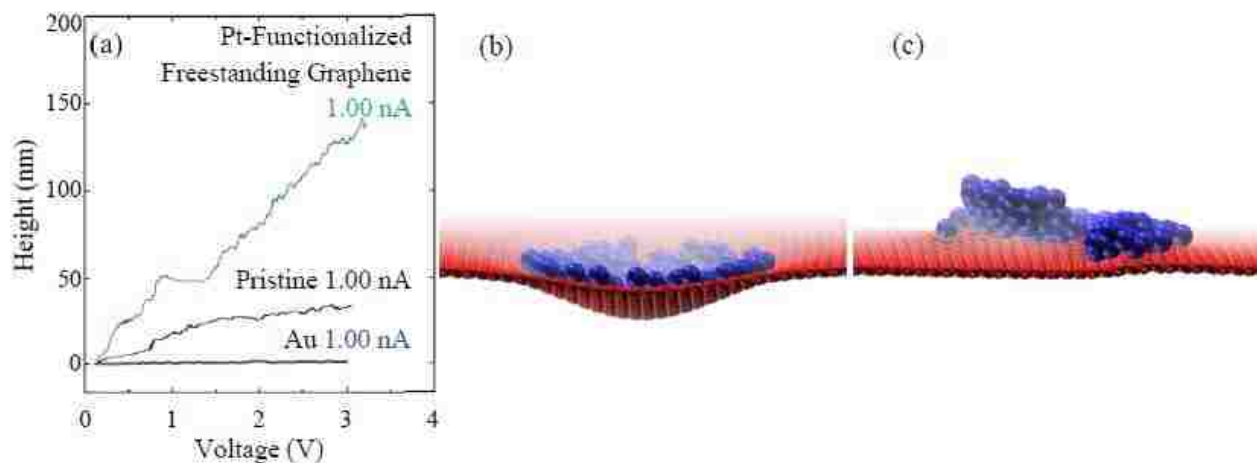
Figure 19: (a) STM tip height versus bias voltage measurements taken at a setpoint current of 1.00 nA for the Pt-functionalized graphene (top curve), pristine freestanding graphene (middle curve), and inflexible Au (bottom curve). (b) Depiction of Pt atoms on graphene inside an initial Gaussian depression. (c) After MD relaxation the previous curvature in the graphene sheet disappeared, and the Pt NP resides on top of a flat graphene surface.

B. DISCUSSION AND CONCLUSIONS

Using the model presented in Chapter 4, we estimate an electrostatic force between the STM tip and the sample to be a few nano-Newtons. This force is pulling on the NP-graphene system and causing it to move toward the STM tip, and since these displacements are fully reversible and repeatable, we can conclude that this force is not large enough to detach a Pt NP from the freestanding graphene surface. This is consistent with the strong covalent bond predicted by our MD simulations. In addition, with the Pt covalently bonded to the surface, the local bonding of the graphene is altered from sp^2 to partial sp^3. This causes the surface curvature to be convex and slightly elevates the Pt NP. Furthermore, the local sp^3 bonding softens the graphene perpendicular to the surface (i.e., the same direction of the applied electrostatic force) and explains the lower voltage needed to reach a 30 nm displacement for the Pt-functionalized film compared to pristine. The important finding here is that the graphene sheet is easier to distort in the presence of Pt NPs, which we deduced from the larger movement in the STS measurements. Generally, the presence of Pt NPs enhances the roughness of graphene and causes the formation of extra ripples, which results in non-uniform carbon-carbon bonds and a non-uniform strain in the membrane. The latter is due to the partial sp^3 hybridization between some Pt atoms and makes the graphene weaker[98].

Due to the surprising nature of the result, our collaborators performed extra MD simulations to further confirm that the graphene surface elevates the Pt NPs rather than wraps around them. They formed a Gaussian-shaped depression in freestanding graphene and filled it with Pt atoms as shown in Fig. 19b. After MD relaxation, the initial concave curvature in the graphene surface disappears and even becomes slightly convex. Note that the original concave curvature in graphene is stable in the absence of Pt, so this significant change in the deformation is due to the

Pt NP. The height of the Pt atoms is not uniform everywhere, which is consistent with the experimental results shown in Fig. 17. The overall self-assembled geometry is due to the preference of forming more covalent bonds between Pt-Pt, rather than Pt-C. Only two or three Pt-C bonds are preferred due to the competition with the elastic energy of graphene. Generally, when weaker van der Waals interactions are dominant, the graphene tends to wrap around the NP, while when stronger covalent bands are involved the elevation occurs.

The elevated feature of the Pt NP also helps to explain the self-organization previously discussed in relation to Fig. 16. During the deposition process, Pt atoms and possibly small clusters are ejected from the target and land on the graphene membrane. The subsequent diffusion is a complex process, influenced by many factors such as temperature and local curvature of the graphene sheet[99]. Essentially, however, the atoms randomly interrogate a region of the surface until they encounter other Pt particles and nucleate into an island. As more Pt atoms arrive on the surface, the island grows. At a certain island size, covalent bonded anchors significantly alter the local bonding and the surface curvature due to the flexibility of the substrate. This in turn creates a local strain field in the immediate vicinity of the NP. Future Pt material therefore avoids these areas and preferentially migrates to other pristine regions of the surface. This process is somewhat similar to the self-organization of semiconductor quantum dot formation in strained thin film growth[100], or to the diffusion of gallium (Ga) atoms under an arsenic (As) flux to form islands of a certain size and density on the surface of GaAs[101]. In our system, the Pt NPs interact with freestanding graphene in such a way as to repel each other over distances of a few nanometers and automatically limit the growth, resulting in uniform coverage across the sample but with a preferred size and nearest-neighbor separation.

VI. SUMMARY

The scanning tunneling microscope is a versatile and well-established instrument in condensed matter physics, and the use of it on flexible 2D surfaces opens up exciting new possibilities. In this work I have explored some of these possibilities with both pristine and functionalized freestanding graphene. When imaging pristine graphene, large corrugation amplitudes were observed which were an order of magnitude larger than the electronic corrugations in the LDOS of graphene. I demonstrated that there existed a significant electrostatic attraction between the voltage-biased STM tip and the grounded sample. The net result of this attraction and the oppositely directed elastic restoring force co-oscillated with the LDOS resulting in the enhanced corrugation. This interplay between the electric and elastic force indicated that the STM can be used to probe both properties in our experiments.

Single point constant-current spectroscopy experiments were performed on the pristine freestanding graphene. In these measurements the tip bias was increased in steps, resulting in a momentarily increased attraction between the graphene and the tip and movement of the graphene towards the tip. The feedback circuit was left on, and the decreased separation between the tip and the graphene resulted in the tip being pulled away from the sheet. In this manner, the graphene sheet was displaced step-by-step with the equilibrium displacement recorded at each voltage. A simple electrostatic model was built in order to easily calculate the magnitude of the electrostatic attraction as a function of tip bias. Combined with the experimental displacement vs. bias measurements, physically transparent force vs. displacement plots were generated for the freestanding graphene.

Finally, STM images and STS measurements, along with TEM images and MD simulations, were used to characterize freestanding graphene sheets functionalized with platinum

nanoparticles. The TEM images revealed the size of the nanoparticles as well as their self-organized periodic arrangment on the graphene. STM images showed that the graphene did not fully encapsulate the nanoparticles and was locally strained by the prescence of the platinum. MD simulations demonstrated that each nanoparticle likely formed 2 -3 sp^3 type covalent bonds with carbon atoms beneath them, anchoring the nanoparticles to the graphene and generating a local strain field that is the likely cause of the self-organization. The strong bonding between the nanoparticles and the graphene was experimentally confirmed by constant-current STS measurements. In the future, these STS measurements could be used as a powerful yet simple diagnostic tool for probing the interface between freestanding graphene and other functionalization groups.

References

[1]   K. S. Novoselov, A. K. Geim, S. V. Morozov, D. Jiang, Y. Zhang, S. V. Dubonos, I. V. Grigorieva, and A. A. Firsov, Science **306**, 666 (2004).

[2]   P. R. Wallace, Phys. Rev. **71**, 622 (1947).

[3]   G. W. Semenoff, Physical Review Letters **53**, 2449 (1984).

[4]   S. V. Morozov, K. S. Novoselov, M. I. Katsnelson, F. Schedin, D. C. Elias, J. A. Jaszczak, and A. K. Geim, Physical Review Letters **100**, 016602 (2008).

[5]   E. V. Castro, H. Ochoa, M. I. Katsnelson, R. V. Gorbachev, D. C. Elias, K. S. Novoselov, A. K. Geim, and F. Guinea, Phys. Rev. Lett. **105**, 266601, 266601 (2010).

[6]   A. S. Mayorov *et al.*, Nano Lett. **11**, 2396 (2011).

[7]   A. A. Balandin, S. Ghosh, W. Bao, I. Calizo, D. Teweldebrhan, F. Miao, and C. N. Lau, Nano Lett. **8**, 902 (2008).

[8]   C. Lee, X. Wei, J. W. Kysar, and J. Hone, Science **321**, 385 (2008).

[9]   J. S. Bunch, S. S. Verbridge, J. S. Alden, A. M. van der Zande, J. M. Parpia, H. G. Craighead, and P. L. McEuen, Nano Lett. **8**, 2458 (2008).

[10]   L. D. Landau, edited by E. M. Lifshitz (Pergamon, Oxford, 1980).

[11]   N. D. Mermin, Physical Review **176**, 250 (1968).

[12]   J. C. Meyer, A. K. Geim, M. I. Katsnelson, K. S. Novoselov, T. J. Booth, and S. Roth, Nature **446**, 60 (2007).

[13]   K. S. Novoselov, D. Jiang, F. Schedin, T. J. Booth, V. V. Khotkevich, S. V. Morozov, and A. K. Geim, Proc. Natl. Acad. Sci. USA **102**, 10451 (2005).

[14]   A. H. Castro Neto, F. Guinea, N. M. R. Peres, K. S. Novoselov, and A. K. Geim, Rev. Mod. Phys. **81**, 109 (2009).

[15]   N. W. Ashcroft, edited by N. D. Mermin (Saunders College, Philadelphia, 1976).

[16]   K. S. Novoselov, A. K. Geim, S. V. Morozov, D. Jiang, M. I. Katsnelson, I. V. Grigorieva, S. V. Dubonos, and A. A. Firsov, Nature **438**, 197 (2005).

[17]   Y. Zhang, Y.-W. Tan, H. L. Stormer, and P. Kim, Nature **438**, 201 (2005).

[18]   M. I. Katsnelson, K. S. Novoselov, and A. K. Geim, Nature Physics **2**, 620 (2006).

[19]   J. C. Meyer, A. K. Geim, M. I. Katsnelson, K. S. Novoselov, D. Obergfell, S. Roth, C. Girit, and A. Zettl, Solid State Commun. **143**, 101 (2007).

[20]   R. Zan *et al.*, Nanoscale **4** (2012).

[21]   S. V. Morozov, K. S. Novoselov, M. I. Katsnelson, F. Schedin, L. A. Ponomarenko, D. Jiang, and A. K. Geim, Phys. Rev. Lett. **97**, 016801 (2006).

[22]   N. Levy, S. A. Burke, K. L. Meaker, M. Panlasigui, A. Zettl, F. Guinea, A. H. Castro Neto, and M. F. Crommie, Science **329**, 544 (2010).

[23]   V. M. Pereira and A. H. Castro Neto, Phys. Rev. Lett. **103**, 046801 (2009).

[24]   A. K. Geim and K. S. Novoselov, Nature Mater. **6**, 183 (2007).

[25]   P. W. Sutter, J.-I. Flege, and E. A. Sutter, Nat Mater **7**, 406 (2008).

[26]   A. Reina, X. Jia, J. Ho, D. Nezich, H. Son, V. Bulovic, M. S. Dresselhaus, and J. Kong, Nano Letters **9**, 30 (2008).

[27]   S. Bae *et al.*, Nature Nanotech. **5**, 574 (2010).

[28]   W. A. de Heer, C. Berger, M. Ruan, M. Sprinkle, X. Li, Y. Hu, B. Zhang, J. Hankinson, and E. Conrad, Proc. Natl. Acad. Sci. USA **108**, 16900 (2011).

[29]   S. Stankovich, D. A. Dikin, R. D. Piner, K. A. Kohlhaas, A. Kleinhammes, Y. Jia, Y. Wu, S. T. Nguyen, and R. S. Ruoff, Carbon **45**, 1558 (2007).

[30]   J. S. Bunch, A. M. van der Zande, S. S. Verbridge, I. W. Frank, D. M. Tanenbaum, J. M. Parpia, H. G. Craighead, and P. L. McEuen, Science **315**, 490 (2007).

[31]   X. Li, Y. Zhu, W. Cai, M. Borysiak, B. Han, D. Chen, R. D. Piner, L. Colombo, and R. S. Ruoff, Nano Letters **9**, 4359 (2009).

[32]   Y. Zhang, V. W. Brar, C. Girit, A. Zettl, and M. F. Crommie, Nature Phys. **5**, 722 (2009).
[33]   S. Fratini and F. Guinea, Phys. Rev. B **77**, 195415 (2008).

[34]   K. I. Bolotin, K. J. Sikes, Z. Jiang, M. Klima, G. Fudenberg, J. Hone, P. Kim, and H. L. Stormer, Solid State Commun. **146**, 351 (2008).

[35]   W. Bao, F. Miao, Z. Chen, H. Zhang, W. Jang, C. Dames, and C. N. Lau, Nature Nanotech. **4**, 562 (2009).

[36]   I. W. Frank, D. M. Tanenbaum, A. M. van der Zande, and P. L. McEuen, J. Vac. Sci. Technol. B **25**, 2558 (2007).

[37]   M. H. Gass, U. Bangert, A. L. Bleloch, P. Wang, R. R. Nair, and A. K. Geim, Nature Nanotech. **3**, 676 (2008).

[38]   G. Binning, H. Rohrer, C. Gerber, and E. Weibel, Physical Review Letters **49**, 57 (1982).

[39]   G. Binnig, H. Rohrer, C. Gerber, and E. Weibel, Applied Physics Letters **40**, 178 (1982).

[40]   C. Bai, (Springer-Verlag, Germay, 2000).

[41]   G. Binnig, H. Rohrer, C. Gerber, and E. Weibel, Physical Review Letters **50**, 120 (1983).

[42]   J. V. Barth, H. Brune, G. Ertl, and R. J. Behm, Physical Review B **42**, 9307 (1990).

[43]   V. P. LaBella, H. Yang, D. W. Bullock, P. M. Thibado, P. Kratzer, and M. Scheffler, Phys. Rev. Lett. **83**, 2989 (1999).

[44]   J. W. G. Wildoer, L. C. Venema, A. G. Rinzler, R. E. Smalley, and C. Dekker, Nature **391**, 59 (1998).

[45]   R. M. Feenstra, J. A. Stroscio, and A. P. Fein, Surface Science **181**, 295 (1987).

[46]   F. M. Chua, Y. Kuk, and P. J. Silverman, Physical Review Letters **63**, 386 (1989).

[47]   L. Feng, C. Z. Hu, and J. D. Andrade, Journal of Microscopy-Oxford **152**, 811 (1988).

[48]   D. P. E. Smith, A. Bryant, C. F. Quate, J. P. Rabe, C. Gerber, and J. D. Swalen, Proceedings of the National Academy of Sciences of the United States of America **84**, 969 (1987).

[49]   R. M. Feenstra, J. A. Stroscio, J. Tersoff, and A. P. Fein, Phys. Rev. Lett. **58**, 1192 (1987).

[50]   D. M. Eigler and E. K. Schweizer, Nature **344**, 524 (1990).

[51]   J. A. Stroscio and D. M. Eigler, Science **254**, 1319 (1991).

[52]   J. Bardeen, Physical Review Letters **6**, 57 (1961).

[53]   J. Tersoff and D. R. Hamann, Phys. Rev. Lett. **50**, 1998 (1983).

[54]   C. J. Chen, Physical Review B **42**, 8841 (1990).

[55]   N. D. Lang, Physical Review Letters **55**, 230 (1985).

[56]   N. D. Lang, Physical Review Letters **56**, 1164 (1986).

[57]   M. Tsukada, K. Kobayashi, and S. Ohnishi, Journal of Vacuum Science & Technology a-Vacuum Surfaces and Films **8**, 160 (1990).

[58]   K. Kobayashi and M. Tsukada, Journal of Vacuum Science & Technology a-Vacuum Surfaces and Films **8**, 170 (1990).

[59]   W. A. Hofer and J. Redinger, Surface Science **447**, 51 (2000).

[60]   J. G. Simmons, Journal of Applied Physics **34**, 1793 (1963).

[61]   N. D. Lang, Physical Review B **37**, 10395 (1988).

[62]   M. C. Payne and J. C. Inkson, Surface Science **159**, 485 (1985).

[63]   J. H. Coombs, M. E. Welland, and J. B. Pethica, Surface Science **198**, L353 (1988).

[64]   J. A. Stroscio, R. M. Feenstra, and A. P. Fein, Physical Review Letters **57**, 2579 (1986).

[65]   J. K. Schoelz, P. Xu, S. D. Barber, D. Qi, M. L. Ackerman, G. Basnet, C. T. Cook, and P. M. Thibado, J. Vac. Sci. Technol. B **30**, 033201 (2012).

[66]   M. Klein and G. Schwitzgebel, Rev. Sci. Instrum. **68**, 3099 (1997).

[67]   M. Kulawik, M. Nowicki, G. Thielsch, L. Cramer, H.-P. Rust, H.-J. Freund, T. P. Pearl, and P. S. Weiss, Rev. Sci. Instrum. **74**, 1027 (2003).

[68]   G. Basnet, J. K. Schoelz, P. Xu, S. D. Barber, M. L. Ackerman, and P. M. Thibado, Journal of Vacuum Science & Technology B **31**, 043201 (2013).

[69]   L. A. Hockett and S. E. Creager, Rev. Sci. Instrum. **64**, 263 (1993).

[70]   P. Xu, Y. Yang, S. D. Barber, M. L. Ackerman, J. K. Schoelz, I. A. Kornev, S. Barraza-Lopez, L. Bellaiche, and P. M. Thibado, Phys. Rev. B **84**, 161409(R) (2011).

[71]   J. M. Soler, A. M. Baro, N. García, and H. Rohrer, Phys. Rev. Lett. **57**, 444 (1986).

[72]   P. E. Blöchl, Phys. Rev. B **50**, 17953 (1994).

[73]   G. Kresse and J. Furthmüller, Comput. Mater. Sci. **6**, 15 (1996).

[74]   R. S. Becker, J. A. Golovchenko, and B. S. Swartzentruber, Physical Review Letters **55**, 987 (1985).

[75]   G. Binnig, K. H. Frank, H. Fuchs, N. Garcia, B. Reihl, H. Rohrer, F. Salvan, and A. R. Williams, Physical Review Letters **55**, 991 (1985).

[76]   J. P. Ibe, P. P. Bey, S. L. Brandow, R. A. Brizzolara, N. A. Burnham, D. P. DiLella, K. P. Lee, C. R. K. Marrian, and R. J. Colton, J. Vac. Sci. Technol. A **8**, 3570 (1990).

[77]   W. R. Smythe, *Static and Dynamic Electricity* (McGraw-Hill Book Company, New York, 1939).

[78]   F. F. Dall'Agnol and V. P. Mammana, Rev. Bras. Ensino Fís. **31**, 3503 (2009).
[79]   H. C. Hamaker, Physica **4**, 1058 (1937).

[80]   V. M. Pereira, A. H. Castro Neto, H. Y. Liang, and L. Mahadevan, Phys. Rev. Lett. **105**, 156603 (2010).

[81]   W. H. Duan and C. M. Wang, Nanotechnology **20**, 075702 (2009).

[82]   A. A. Pacheco Sanjuan, Z. Wang, H. P. Imani, M. Vanević, and S. Barraza-Lopez, Physical Review B **89**, 121403 (2014).

[83]   F. Guinea, Solid State Communications **152**, 1437 (2012).

[84]   B. C. H. Steele and A. Heinzel, Nature **414**, 345 (2001).

[85]   K. Yamamoto, T. Imaoka, W. J. Chun, O. Enoki, H. Katoh, M. Takenaga, and A. Sonoi, Nature Chemistry **1**, 397 (2009).

[86]   R. Siburian, T. Kondo, and J. Nakamura, Journal of Physical Chemistry C **117**, 3635 (2013).

[87]   P. Costamagna and S. Srinivasan, Journal of Power Sources **102**, 242 (2001).

[88]   W. Z. Li, C. H. Liang, W. J. Zhou, J. S. Qiu, Z. H. Zhou, G. Q. Sun, and Q. Xin, Journal of Physical Chemistry B **107**, 6292 (2003).

[89]   L. F. Dong, R. R. S. Gari, Z. Li, M. M. Craig, and S. F. Hou, Carbon **48**, 781 (2010).

[90]   B. Seger and P. V. Kamat, Journal of Physical Chemistry C **113**, 7990 (2009).

[91]   Y. A. Tang, Z. X. Yang, and X. Q. Dai, Physical Chemistry Chemical Physics **14**, 16566 (2012).

[92]   K. Okazaki-Maeda, Y. Morikawa, S. Tanaka, and M. Kohyama, Surface Science **604**, 144 (2010).

[93]   V. Kumar and Y. Kawazoe, Physical Review B **77**, 205418 (2008).

[94]   Y. Okamoto, Chemical Physics Letters **420**, 382 (2006).

[95]   R. Wiesendanger, *Scanning Probe Microscopy and Spectroscopy: Methods and Applications* (Cambridge University Press, 1994)

[96]   J. M. Yuk, J. Park, P. Ercius, K. Kim, D. J. Hellebusch, M. F. Crommie, J. Y. Lee, A. Zettl, and A. P. Alivisatos, Science **336**, 61 (2012).

[97]   N. Mohanty, M. Fahrenholtz, A. Nagaraja, D. Boyle, and V. Berry, Nano Lett. **11**, 1270 (2011).

[98]   M. Neek-Amal, R. Asgari, and M. R. R. Tabar, Nanotechnology **20**, 135602 (2009).

[99]   L. Liu, Z. Y. Chen, L. Wang, E. Polyakova, T. Taniguchi, K. Watanabe, J. Hone, G. W. Flynn, and L. E. Brus, Journal of Physical Chemistry B **117**, 4305 (2013).

[100]   P. Venezuela, J. Tersoff, J. A. Floro, E. Chason, D. M. Follstaedt, F. Liu, and M. G. Lagally, Nature **397**, 678 (1999).

[101]   H. Yang, V. P. Labella, D. W. Bullock, and P. M. Thibado, Journal of Vacuum Science & Technology B **17**, 1778 (1999).

Appendix A: Summary of Electrostatic Equations for the Sphere-Plane Model

Initial Charge	$$q_0 = 4\pi\epsilon_0 aV = \frac{aV}{k}$$
Position of Initial Charge	$$z_0 = a + s$$
Magnitude of nth Charge	$$\bar{q}_n = \frac{q_n}{q_0} = \frac{aq_{n-1}}{z_0 + z_{n-1}}, \quad n > 0$$
Position of nth Charge	$$z_n = z_0 - \frac{a^2}{z_0 + z_{n-1}}, \quad n > 0$$
Exterior Potential	$$\Phi(\boldsymbol{r}) = aV \sum_{n=0}^{\infty} \left[\frac{\bar{q}_n}{\sqrt{\rho^2 + (z - z_n)^2}} - \frac{\bar{q}_n}{\sqrt{\rho^2 + (z + z_n)^2}} \right]$$
Radial Field	$$E_\rho = -\frac{\partial\Phi}{\partial\rho} = aV\rho \sum_{n=0}^{\infty} \left[\frac{\bar{q}_n}{[\rho^2 + (z - z_n)^2]^{3/2}} - \frac{\bar{q}_n}{[\rho^2 + (z + z_n)^2]^{3/2}} \right]$$
Perpendicular Field	$$E_z = -\frac{\partial\Phi}{\partial z} = aV \sum_{n=0}^{\infty} \left[\frac{\bar{q}_n(z - z_n)}{[\rho^2 + (z - z_n)^2]^{3/2}} - \frac{\bar{q}_n(z + z_n)}{[\rho^2 + (z + z_n)^2]^{3/2}} \right]$$
Induced Charge on Plane	$$\sigma(\rho) = \epsilon_0 E_z|_{z=0} = -2\epsilon_0 aV \sum_{n=0}^{\infty} \frac{\bar{q}_n z_n}{(\rho^2 + z_n{}^2)^{3/2}}$$
Electrostatic Energy	$$U = \frac{1}{2} \sum_{n=0}^{\infty} q_n\phi_n = \frac{aV^2}{2k} \sum_{n=0}^{\infty} \bar{q}_n$$
Derivative of nth Charge Magnitude	$$\frac{d\bar{q}_n}{dz_0} = \bar{q}_n' = \frac{a\bar{q}_{n-1}'}{z_0 + z_{n-1}} - \frac{aq_{n-1}'}{z_0 + z_{n-1}} \frac{1 + z_{n-1}'}{z_0 + z_{n-1}}, \quad \bar{q}_0' = 0$$

Derivative of nth Charge Position	$$\frac{dz_n}{dz_0} = z'_n = 1 + \frac{a^2}{z_0 + z_{n-1}} \frac{1 + z'_{n-1}}{z_0 + z_{n-1}}, \quad z'_0 = 1$$
Electrostatic Force	$$F = -\frac{dU}{dz_0} = -\frac{aV^2}{2k} \sum_{n=1}^{\infty} \bar{q}'_n$$

Appendix B: Mathematica 9.0 Code for Sphere-Plane Model

Charges and Derivatives

"Sphere-Plane Model. SI. This routine computes the image charge q, charge position d, charge

derivative dq, and position derivative dd values for a given sphere radius a and sphere-plane

separation s. The ordered values are then exported in .csv files.";

Clear[a,s,nter,d0,d,dd,q,dq,r,dr,S,DS,Z,DZ];

"Input Parameters";

a=20*10^-9;"Sphere radius in meters";

s=0.5*10^-9;"Sphere-plane separation in meters";

nter=150;"Number of image charges to compute";

"Derived Quantities";

d0=a+s;"z coordinate of the sphere center";

d[0]=d0;"Position of first charge";

dd[0]=1; "First position derivative";

q[0]=1;"Magnitude of first charge";

dq[0]=0;"First charge derivative";

Do[r[i]=a/(d0+d[i-1]);dr[i]=r[i]^2*(1+dd[i-1]);d[i]=d0-a*r[i];q[i]=r[i]*q[i-

1];dd[i]=1+dr[i];dq[i]=dq[i-1]*r[i]-q[i-1]*dr[i]/a,{i,1,nter}]

```
Q=Table[q[i],{i,0,nter}];

DQ=Table[dq[i],{i,0,nter}];

Z=Table[d[i],{i,0,nter}];

DZ=Table[dd[i],{i,0,nter}];


Export["q.csv",{Q}]

Export["qprime.csv",{DQ}]

Export["z.csv",{Z}]

Export["zprime.csv",{DZ}]
```

Potential

"Sphere-Plane Model. SI. This routine computes the electric potential V for a given sphere radius

a, sphere-plane separation s, and bias v at the point (x,y,z).";

Clear[a,s,x,y,z,v,nter,d0,d,q,r,V];

"Input Parameters";

a=20*10^-9;"Sphere radius in meters";

s=0.5*10^-9;"Sphere-plane separation in meters";

x=0;y=0;z=0; "(x,y,z) evaluation point";

v=1;"Tip bias";

nter=150;"Number of image charges to compute";

"Derived Quantities";

d0=a+s;"z coordinate of the sphere center";

d[0]=d0;"Position of first charge";

q[0]=1;"Magnitude of first charge";

Do[r[i]=a/(d0+d[i-1]);d[i]=d0-a*r[i];q[i]=r[i]*q[i-1],{i,1,nter}]

V=a*v*Sum[q[i]*((x^2+y^2+(z-d[i])^2)^-(1/2)-(x^2+y^2+(z+d[i])^2)^-(1/2)),{i,0,nter}]

Radial Component of the Electric Field

"Sphere-Plane Model. SI. This routine computes the radial component of the electric field Er for

a given sphere radius a, sphere-plane separation s, and bias v at the point (x,y,z).";

Clear[a,s,x,y,z,v,nter,d0,d,q,r,Er];

"Input Parameters";

a=20*10^-9;"Sphere radius in meters";

s=0.5*10^-9;"Sphere-plane separation in meters";

x=10;y=0;z=0; "(x,y,z) evaluation point";

v=1;"Tip bias";

nter=150;"Number of image charges to compute";

"Derived Quantities";

d0=a+s;"z coordinate of the sphere center";

d[0]=d0;"Position of first charge";

q[0]=1;"Magnitude of first charge";

Do[r[i]=a/(d0+d[i-1]);d[i]=d0-a*r[i];q[i]=r[i]*q[i-1],{i,1,nter}]

Er=a*v*(x^2+y^2)^(1/2)Sum[q[i]*((x^2+y^2+(z-d[i])^2)^-(3/2)-(x^2+y^2+(z+d[i])^2)^-

(3/2)),{i,0,nter}]

Perpendicular Component of the Electric Field

"Sphere-Plane Model. SI. This routine computes the component of the electric field

perpendicular to the plane Ez for a given sphere radius a, sphere-plane separation s, and bias v at

the point (x,y,z).";

Clear[a,s,x,y,z,v,nter,d0,d,q,r,Ez];

"Input Parameters";

a=20*10^-9;"Sphere radius in meters";

s=0.5*10^-9;"Sphere-plane separation in meters";

x=10;y=0;z=0; "(x,y,z) evaluation point";

v=1;"Tip bias";

nter=150;"Number of image charges to compute";

"Derived Quantities";

d0=a+s;"z coordinate of the sphere center";

d[0]=d0;"Position of first charge";

q[0]=1;"Magnitude of first charge";

Do[r[i]=a/(d0+d[i-1]);d[i]=d0-a*r[i];q[i]=r[i]*q[i-1],{i,1,nter}]

Ez=a*v*Sum[q[i]*((z-d[i])*(x^2+y^2+(z-d[i])^2)^-(3/2)-(z+d[i])*(x^2+y^2+(z+d[i])^2)^-

(3/2)),{i,0,nter}]

Induced Surface Charge Distribution in the Plane

"Sphere-Plane Model. SI. This routine computes the charge density sigma on the plane for a given sphere radius a, sphere-plane separation s, and bias v as a function of radial distance from the origin. The charge density is computed out to a radial distance p in nstep equal steps at evaluation points dp. The (dp,sigma) data is exported in a .csv file.";

Clear[a,s,p,nstep,v,nter,d0,d,q,r,sigma,dp,n];

"Input Parameters";

a=20*10^-9;"Sphere radius in meters";

s=0.5*10^-9;"Sphere-plane separation in meters";

p=10^-7; "Radial distance of computation";

nstep=500; "Step size is p/nstep";

v=1;"Tip bias";

nter=150;"Number of image charges to compute";

"Derived Quantities";

d0=a+s;"z coordinate of the sphere center";

d[0]=d0;"Position of first charge";

q[0]=1;"Magnitude of first charge";

dp=N[Table[p*n/nstep,{n,0,nstep}]]; "Points of evaluation";

Do[r[i]=a/(d0+d[i-1]);d[i]=d0-a*r[i];q[i]=r[i]*q[i-1],{i,1,nter}]

```
sigma=-2*8.854187817*10^-12*a*v*Sum[q[i]*d[i]*(dp^2+d[i]^2)^-(3/2),{i,0,nter}];
```

```
Export["sigma.csv",{dp,sigma}]
```

Electrostatic Force

"Sphere-Plane Model. SI. This routine computes the electrostatic attraction for a given sphere

radius a and sphere-plane separation s and tip bias v";

Clear[a,s,v,nter,d0,d,dd,q,dq,r,dr,F];

"Input Parameters";

a=20*10^-9;"Sphere radius in meters";

s=0.5*10^-9;"Sphere-plane separation in meters";

v=1;"Tip bias";

nter=150;"Number of image charges to compute";

"Derived Quantities";

d0=a+s;"z coordinate of the sphere center";

d[0]=d0;"Position of first charge";

dd[0]=1; "First position derivative";

q[0]=1;"Magnitude of first charge";

dq[0]=0;"First charge derivative";

Do[r[i]=a/(d0+d[i-1]);dr[i]=r[i]^2*(1+dd[i-1]);d[i]=d0-a*r[i];q[i]=r[i]*q[i-

1];dd[i]=1+dr[i];dq[i]=dq[i-1]*r[i]-q[i-1]*dr[i]/a,{i,1,nter}]

F=a*v^2*2*Pi*8.854187817*10^-12*Sum[dq[i],{i,nter}]

Appendix C: Numerical Evaluation of the Electrostatic Force in the Sphere-Plane Model

Numerical Evaluation of $\bar{Q}'(s;a)$

The electrostatic force in the sphere-plane model depends on the term

$$\bar{Q}' = \sum q_n'(s;a)$$

which is a function of the sphere-plane separation s and depends parametrically on the sphere radius a. In order to determine the functional dependence of $\bar{Q}'$ on s, the sum was numerically evaluated for values of s ranging from 0.1 to 5,000 pm in 0.1 pm steps for our standard parameter value a = 20 nm. Because of the evident power law nature of the result, the data is also plotted in a log-log plot. The linear log-log plot was fitted using a least-squares method in Mathematica (see Appendix D) which yielded the relationship

$$\bar{Q}'(s) \simeq 0.1264 * s^{-1.061}.$$

Numerical Evaluation of $F(V;I)$

The change in the tip-sample separation with tip bias in the $z(V)$ measurements on freestanding graphene cannot be measured directly. The $z(V)$ measurements taken on the stationary graphene sample (shown in Fig. 8) are assumed to give the movement of the tip relative to the sample which is intrinsic to graphene, and therefore reveal the $s(V)$ relationship in the freestanding graphene measurements. Accordingly, the data in Fig. 8 were fitted using a B-spline function $f(V;I)$ with a polynomial basis of degree 3 in Mathematica using the experimental data points as knots. This yielded three functions, one for each setpoint current, and we can now state

$$\bar{Q}'(V;I) \simeq 0.1264 * [s_0 + f(V;I)]^{-1.061}$$

where I = 0.01, 0.1, or 1.0 nA and s_0 is assumed to be 0.5 nm. The electrostatic attraction between the sphere and plane is now

$$F(V; I) = \frac{aV^2}{2k} \bar{Q}'(V; I).$$

Code implementing this procedure in Mathematica is shown in Appendix D.

Appendix D: Mathematica 9.0 Code for Numerical Evaluation of the Electrostatic Force in the Sphere-Plane Model

Numerical Evaluation of $\bar{Q}'(s;a)$

"Sphere-Plane Model. SI. This routine computes the sum of the charge derivatives Q for a given sphere radius a and for a series of sphere-plane separations s. The initial separation is s0, the separation step size is ds, and the number of points evaluated is nstep. The (s,Q) data is exported in a .csv file. Log-log data, (Log[s],Log[Q]), is also exported in a .csv file. The log-log data is given a linear fit Log[Q]=b*Log[s]+c such that the functional relationship between the variables is Q=Exp[c]*s^b.";

Clear[a,s,s0,ds,nstep,nter,d0,d,dd,q,dq,r,dr,Q,data,logdata];

"Input Parameters";

a=20*10^-9;"Sphere radius in meters";

s0=0.0001*10^-9;"Initial sphere-plane separation in meters";

ds=s0;"Step size";

nstep=50000;"Number of evaluations";

nter=150;"Number of image charges to compute";

"Derived Quantities";

s=N[Table[s0+n*ds,{n,0,nstep-1}]];

d0=a+s;"z coordinate of the sphere center";

d[0]=d0;"Position of first charge";

dd[0]=1; "First position derivative";

q[0]=1;"Magnitude of first charge";

dq[0]=0;"First charge derivative";

Do[r[i]=a/(d0+d[i-1]);dr[i]=r[i]^2*(1+dd[i-1]);d[i]=d0-a*r[i];q[i]=r[i]*q[i-1];dd[i]=1+dr[i];dq[i]=dq[i-1]*r[i]-q[i-1]*dr[i]/a,{i,1,nter}]

Q=-Sum[dq[i],{i,nter}];

data=Table[{s[[i]],Q[[i]]},{i,1,nstep}];

logdata=Table[{Log[s[[i]]],Log[Q[[i]]]},{i,1,nstep}];

Fit[logdata,{1,x},x]

Export["data.csv",data]

Export["logdata.csv",logdata]

Numerical Evaluation of $F(V; I)$

"Sphere-Plane Model. SI. This routine imports the experimental s(V) data taken on a stationary graphene sample and generates a B-spline function s(V) using the data points as knots. The function F(V) is then generated using the relationship F(V)=(aV^2/2k)*b*(s0+s(V))^c where b and c are parameters which depend on the sphere radius a and are calculated by the routine Q.nb and s0 is the initial tip-sample separation. The function F(V) is evaluated along 10,000 data points and the (V,F) data is exported as a .csv file." ;

Clear[data,filename,f,a,b,c,V,v,F,vmin,vmax,s,table];

"Input Parameters";

a=20*10^-9;"Sphere radius in meters";

b=0.1264;

c=-1.061;

s0=0.5*10^-9;"Initial tip-sample separation";

filename="1.00nAZV.csv";

data=Import[filename];

v=Table[data[[i,1]],[102]];

vmin=First[v];

vmax=Last[v];

f=BSplineFunction[data];

s=Function[u,10^-9*Last[f[(u-vmin)/(vmax-vmin)]]];

F=Function[V,a*V^2*2*Pi*8.854187817*10^-12*b*(s0+s[V])^c];

table=Table[{i,F[i]},{i,vmin,vmax,(vmax-vmin)/10000}];

Export["force_1.00.csv",table]

Construction of Force-Displacement Curves

"Sphere-Plane Model. SI. This routine calculates F(V) as in the Force_Curve.nb routine. It then imports the freestanding Z(V) data and subtracts the s(V) data from it to get a displacement vs. voltage data set. It then constructs a (displacement, force) data set and exports that data set as a .csv file. That data is then integrated to give the work done on the graphene sheet in eV." ;

Clear[data,filename,f,a,b,c,V,v,F,vmin,vmax,s,table];

"Input Parameters";

a=20*10^-9;"Sphere radius in meters";

b=0.1264;

c=-1.061;

s0=0.5*10^-9;"Initial tip-sample separation";

cudata="0.01nAZV.csv";

fsdata="0.01nAZVfs.csv";

data=Import[cudata];

v=Table[data[[i,1]],[102]];

vmin=First[v];

```
vmax=Last[v];

f=BSplineFunction[data];

s=Function[u,Last[10^-9*f[(u-vmin)/(vmax-vmin)]]];

F=Function[V,a*V^2*2*Pi*8.854187817*10^-12*b*(s0+s[V])^c];


data2=Import[fsdata];

z=Table[10^-9*data2[[i,2]],[102]];

t=Table[data2[[i,1]],[102]];

tmin=First[t];

tmax=Last[t];

s2=Function[u,10^-9*Last[f[(u-tmin)/(tmax-tmin)]]];

d=Table[z[[i]]-s2[t[[i]]],[102]];

F2=Function[V,a*V^2*2*Pi*8.854187817*10^-12*b*(s0+s2[V])^c];

fd=Table[{d[[i]],F2[t[[i]]]},{i,1,Length[data2]}];

Export["0.01Fd.csv",fd]


m=Interpolation[fd];

min=First[d];
```

88

max=Last[d];

Work=NIntegrate[m[x],{x,min,max}]/(1.6*10^-19)